Do AGN triggering mechanisms vary with radio power? I. Optical morphologies of radio-intermediate HERGs

J. C. S. Pierce,[1]* C. N. Tadhunter,[1] C. Ramos Almeida,[2,3] P. S. Bessiere[4] and M. Rose[1]

[1] *Department of Physics and Astronomy, University of Sheffield, Sheffield S3 7RH, UK*
[2] *Instituto de Astrofísica de Canarias, Calle Vía Láctea, s/n, E-38205 La Laguna, Tenerife, Spain*
[3] *Departamento de Astrofísica, Universidad de La Laguna, E-38205 La Laguna, Tenerife, Spain*
[4] *Instituto de Astrofísica, Facultad de Física, Pontificia Universidad Católica de Chile, Casilla 306, Santiago 22, Chile*

ABSTRACT

Radio AGNs with intermediate radio powers are capable of driving multi-phase outflows in galaxy bulges, and are also more common than their high-radio-power counterparts. In-depth characterisation of the typical host galaxies and likely triggering mechanisms for this population is therefore required in order to better understand the role of radio AGN feedback in galaxy evolution. Here, we use deep optical imaging data to study the detailed host morphologies of a complete sample of 30 local radio AGNs with high-excitation optical emission (HERG) spectra and intermediate radio powers ($z < 0.1$; $22.5 < \log(L_{1.4GHz}) < 24.0$ W Hz^{-1}). The fraction of hosts with morphological signatures of mergers and interactions is greatly reduced compared to the 2 Jy radio-powerful galaxies ($\log(L_{1.4GHz}) > 25.0$ W Hz^{-1}) with strong optical emission lines: 53 ± 9 per cent and 94 ± 4 per cent, respectively. In addition, the most radio-powerful half of the sample has a higher frequency of morphological disturbance than the least radio-powerful half (67 ± 12 per cent and 40 ± 13 per cent, respectively), including the eight most highly-disturbed galaxies. This suggests that the importance of triggering nuclear activity in HERGs through mergers and interactions reduces with radio power. Both visual inspection and detailed light profile modelling reveal a mixed population of early-type and late-type morphologies, contrary to the massive elliptical galaxy hosts of radio-powerful AGNs. The prevalence of late-type hosts could suggest that triggering via secular, disk-based processes has increased importance for HERGs with lower radio powers (e.g. disk instabilities, large scale bars).

Key words: galaxies: interactions – galaxies: active – galaxies: nuclei – galaxies: photometry

1 INTRODUCTION

The feedback effects caused by powerful radio jets from active galactic nuclei (AGNs) have rendered them an important component of current models of galaxy evolution. On the scales of individual galaxies, these jets are seen to drive massive outflows of gas in multiple phases (e.g. Morganti et al. 2005a,b; Nesvadba et al. 2006; Holt et al. 2008; Nesvadba et al. 2010; Russell et al. 2017), potentially having a significant influence on star formation in the inner regions of the galaxy and regulating the fuelling of the AGN.

In many radio galaxies, these jets are seen to inflate

larger-scale cavities in the hot interstellar/intracluster gas (ISM/ICM) that can propagate well beyond the extent of the hosts (see McNamara & Nulsen 2007, for a review), also giving their feedback effects importance in a cosmological framework. Since the bright central galaxies in high density galaxy clusters are predominantly radio AGNs (e.g. Best et al. 2007), they are commonly invoked as the solution to the 'cooling flow problem' associated with these environments (Fabian 1994), providing an injection of energy that can counteract the cooling of hot intracluster gas via X-ray emission. This would also restrict the build up of mass in these brightest cluster galaxies (BCGs). Thus, radio AGNs are often considered key to accounting for the lack of observed galaxies at the upper end of galaxy luminosity

---

* E-mail: jcspierce1@sheffield.ac.uk

or stellar mass functions, relative to theoretical predictions (e.g. Bower et al. 2006; Vogelsberger et al. 2014; Croton et al. 2006, 2016).

The heating of the hot ISM/ICM by relativistic jets is commonly implemented into cosmological simulations through the inclusion of 'radio-mode' AGN activity. Best et al. (2006) have demonstrated that this type of feedback is dominated by relatively low radio power sources $(\log(L_{1.4GHz}) \lesssim 24.0 \text{ W Hz}^{-1})$, which often have weak or 'low-excitation' optical emission lines and are labelled as low-excitation radio galaxies (LERGs). Such radio AGNs are thought to be fuelled by radiatively-inefficient accretion flows of hot gas that lead to low black hole accretion rates (e.g. Hardcastle et al. 2007; Best & Heckman 2012).

In contrast, 'quasar mode' AGN activity is commonly assumed to drive broad winds that can heat and expel the warm and cool phases of the ISM in the bulges of the host galaxies. This mode is associated with the radiatively-efficient accretion of cold gas at high black hole accretion rates, resulting in high-excitation optical emission-line spectra. This wind-based feedback may therefore be important for high-excitation radio galaxies (HERGs), which are believed to be fuelled in this way (e.g. Best & Heckman 2012). However, such objects also possess powerful radio jets that are themselves able to heat and expel the ISM in the host galaxies.

Indeed, there is now strong evidence to suggest that the radio jets of HERGs with intermediate radio powers $(22.5 < \log(L_{1.4GHz}) < 25.0 \text{ W Hz}^{-1})$ are capable of causing kinematic disturbances in the multi-phase gas of their host galaxies (Tadhunter et al. 2014; Harrison et al. 2015; Ramos Almeida et al. 2017; Villar-Martín et al. 2017), perhaps even more significantly than those with higher radio powers (Mullaney et al. 2013). In addition, it is evident from the local radio galaxy luminosity function that radio-intermediate AGNs are considerably more common than their counterparts at higher radio powers (Best & Heckman 2012). Detailed characterisation of the population of radio-intermediate HERGs is therefore crucial for investigating the role of radio AGN feedback in galaxy evolution.

In order to correctly implement radio-intermediate HERG feedback into models of galaxy evolution, it is important to know what types of host galaxies they are associated with. At high radio powers, the general population of radio AGN hosts is predominantly composed of elliptical galaxies with high stellar masses (Matthews et al. 1964; Dunlop et al. 2003; Best et al. 2005b; Tadhunter et al. 2011). It is seen, however, that in samples of local radio galaxies selected at high flux densities (e.g. 3CR and 2 Jy), the few that show signs of disk-like components in optical images are typically found towards lower radio powers, and half lie in the radio-intermediate regime (Tadhunter 2016). In addition, it appears that the frequency of late-type hosts could increase at lower radio powers – Sadler et al. (2014) find that 30 per cent of their radio AGN hosts are spiral galaxies at low redshifts (mostly $L_{1.4GHz} \sim 10^{22-23} \text{ W Hz}^{-1}$). Furthermore, Seyfert galaxies, arguably the counterparts of HERGs at the lowest radio powers, are predominantly associated with late-type morphologies (e.g. Adams 1977). Therefore, the radio-intermediate objects are crucial for investigating the possible transition in host galaxy morphologies along the HERG sequence.

In addition, it is important to determine the likely triggering mechanisms for the nuclear activity. Previous deep optical imaging studies of large samples of powerful radio galaxies demonstrate that those with strong optical emission lines commonly show morphological signatures of galaxy mergers at relatively high surface brightnesses (Heckman et al. 1986; Smith & Heckman 1989a,b). Most recently, Ramos Almeida et al. (2011) have shown that 94 ± 4 per cent of the strong-line radio galaxies (SLRGs)[1] in the 2 Jy sample exhibit such tidal features. Comparison with images of control samples of elliptical galaxies matched in absolute magnitude and surface brightness depth also reveals an excess of high-surface-brightness tidal features for the 2 Jy SLRGs relative to the non-active population (Ramos Almeida et al. 2012). The SLRGs also show a preference for group-like environments (Ramos Almeida et al. 2013), which are suitable for frequent galaxy-galaxy collisions without the high relative galaxy velocities found in clusters that might reduce the merger rate (Quinn 1984; Popesso & Biviano 2006). This, amongst other evidence, has led to suggestions that the cold gas necessary for radiatively efficient accretion in HERGs is supplied by mergers and interactions, in line with optically selected AGNs (Croton et al. 2006; Buttiglione et al. 2010; Best & Heckman 2012; Heckman & Best 2014; Mingo et al. 2014).

In contrast to the situation for the high radio power HERGs selected in samples such as the 3CR and 2 Jy, the lack of systematic study of radio-intermediate HERGs means that the typical host galaxies and fuelling mechanisms have not yet been determined for this population. Here, we present the first in a series of papers which use deep optical imaging of local HERGs with intermediate radio powers to investigate the host morphologies and likely triggering mechanisms for their nuclear activity. We use deep images of a complete sample of 30 radio-intermediate HERGs to analyse their detailed optical morphologies, and determine the host galaxy types from both visual inspection and light profile modelling. In §2, we detail the selection of our sample and describe the observations and subsequent data reduction. The analysis of the reduced images and subsequent results are outlined in §3. Our results are discussed in §4, and §5 summarises our work and concludes the study. A cosmology described by $H_0 = 73.0 \text{ km s}^{-1} \text{ Mpc}^{-1}$, $\Omega_m = 0.27$ and $\Omega_\Lambda = 0.73$ is assumed throughout this paper.

2 SAMPLE SELECTION, OBSERVATIONS AND REDUCTION

2.1 Sample selection

The sample was selected from the catalog of 18,286 local radio AGNs produced by Best & Heckman (2012), which comprises all AGN host galaxies within SDSS DR7 (Abazajian et al. 2009) with counterpart radio emission at 1.4 GHz in the FIRST (Becker et al. 1995) and/or NVSS (Condon et al. 1998) surveys. The objects were classified as AGNs based on their SDSS optical emission spectra, which were

---

[1] Strong-line radio galaxies are selected based on [OIII] emission-line equivalent width, but show a strong overlap with the HERG population (see discussion in Tadhunter 2016).

also used to classify the AGNs as either high-excitation or low-excitation radio galaxies (HERGs/LERGs). This latter division is based on either 'excitation index' (EI) from Buttiglione et al. (2010), diagnostic diagrams from Kewley et al. (2006), [OIII] emission line equivalent width, or plots of [NII]/Hα versus [OIII]/Hα from Cid Fernandes et al. (2010) – see Best & Heckman (2012) for further details on the classification. Note that this selection differs from the strong-line/weak-line radio galaxy (SLRG/WLRG) division – based solely on the equivalent width of the [OIII]λ5007 emission line – used in other studies (Tadhunter et al. 1998; Ramos Almeida et al. 2011, 2012, 2013), as is discussed in Tadhunter (2016).

To construct the sample, all AGNs in the catalog with intermediate radio powers in the range $22.5 < \log(\mathrm{L_{1.4GHz}}) < 24.0$ W Hz^{-1} and high-excitation emission spectra (HERGs) were selected. In almost all cases, the radio powers were derived from the measured NVSS fluxes for the targets, to ensure that as little as possible of the radio emission was lost due to resolution effects. The NVSS fluxes could not be used for the targets J0911 and J1358, due to contamination by other radio sources within the resolution limit of the NVSS survey, and so the measured FIRST fluxes were used in these cases. The sample was also restricted to low redshifts ($z < 0.1$) to ensure sensitivity to any low surface brightness tidal features that may be present. The right ascension (α) values for the targets were then restricted to the range 07h 15m $< \alpha <$ 16h 45m, such that the targets could be easily observed in the same observing window. The final sample consists of 30 objects, and provides a large, representative sample of local HERGs with intermediate radio powers that is complete within these constraints – see Table 1 for further information on the individual targets. Although we cannot entirely rule out the contamination of the sample by radio-quiet AGNs in star forming galaxies, we consider this to be unlikely based on the analysis of far-infrared data; see Appendix A.

The radio power and stellar mass distributions for the HERGs in the sample are displayed in Figure 1, with their 25th, 50th (median) and 75th percentiles indicated. The galaxies have stellar masses in the range $10.0 < \log(\mathrm{M_*/M_\odot}) < 11.4$ though are skewed towards higher masses, with a median of $10^{10.8}$ M$_\odot$. The radio power distribution is slightly skewed towards the lower radio luminosities in the range, with a median of $10^{23.06}$ W Hz^{-1}, as expected from the local luminosity function.

2.2 Observations

The deep optical imaging data were obtained on four consecutive nights in 2017 March, using the Wide-Field Camera (WFC) attached to the 2.5m Isaac Newton Telescope (INT) at the Observatorio del Roque de los Muchachos, La Palma. The seeing full width at half maximum (FWHM) ranged between 1.07 and 2.05 arcsec over the course of the observations, with a median of 1.38 arcsec. The individual seeing values for the observations were calculated by the THELI package for astronomical image reduction and processing (see Schirmer 2013, for details), using plots of half-light radius against magnitude for foreground stars in the final coadded images (post-reduction). The first night of observations was photometric, but intermittent thin cloud rendered the
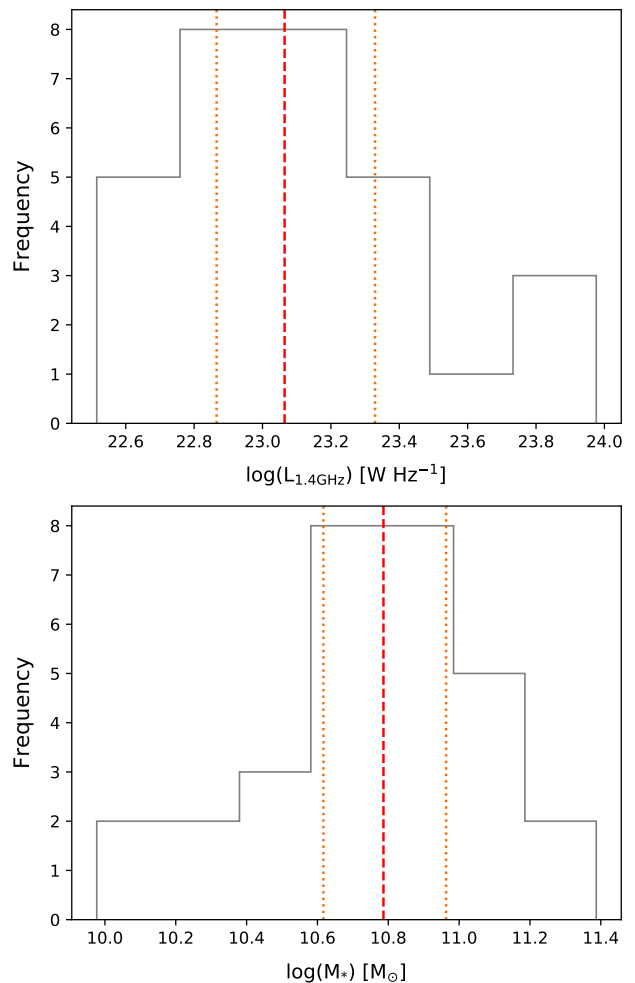
Figure 1. The L$_{1.4GHz}$ radio power (upper panel) and stellar mass (lower panel) distributions for the galaxies in the sample. The median values are indicated by the red dashed lines, whilst the 25th and 75th percentiles are displayed as orange dotted lines.

remaining nights not entirely photometric. Details on the individual target observations are presented in Table 1.

The WFC consists of four thinned, anti-reflection-coated 2048 × 4100 pixel CCDs separated by gaps of $660 - 1098$ μm. With pixel sizes of 0.333 arcsec pixel^{-1}, this provides a large total field-of-view of order 34 × 34 arcmin^2. The images were taken through the WFC Sloan r-band filter (λ_{eff} = 6240 Å, $\Delta\lambda$ = 1347 Å), chosen to be consistent with existing SDSS r'-band observations of our targets (see Fukugita et al. 1996, for further details) and the GMOS-S r'-band ($z < 0.4$) and i'-band ($0.4 < z < 0.7$) observations of radio-loud galaxies in the 2 Jy sample performed by Ramos Almeida et al. (2011). Each target was observed using 4 × 700s exposures, yielding total exposure times of 2800s per target. Such exposure lengths were necessary for the detection of low-surface-brightness tidal features, but were divided into four separate exposures to ensure that the target galaxies were not saturated in individual images. A square dithering pattern was employed to overcome the gaps in the images introduced by the spacings between the CCDs,

Table 1. Basic information for all 30 targets within the observed sample, selected as detailed in §2.1. Column 1 lists the full SDSS IDs for the targets, with their in-text abbreviations included in brackets. Columns 2, 3 and 4 give the spectroscopic redshifts, r-band extinction (in magnitudes) and r-band magnitudes (corrected for extinction) for the targets, as obtained through the SDSS DR7 Object Explorer tool (available at: http://cas.sdss.org/dr7/en/tools/explore/). The r-band extinction values are calculated from the full-sky $100\,\mu$m maps of Schlegel et al. (1998), whilst the raw r-band magnitudes considered are are those given by the best fitting model between standard de Vaucouleurs and exponential profiles. Column 5 denotes the radio luminosities of the galaxies at 1.4 GHz derived from their NRAO VLA Sky Survey (NVSS) fluxes (Condon et al. 1998), or Faint Images of the Radio Sky at Twenty-cm (FIRST) fluxes (Becker et al. 1995) in the cases of J0911 and J1358 (see §2.1). Columns 6 and 7 provide the [OIII] λ5007 luminosities and stellar masses taken from the MPA/JHU value-added catalogue for SDSS DR7 (available at: https://wwwmpa.mpa-garching.mpg.de/SDSS/DR7/). Columns 8 and 9 show the date and the atmospheric seeing for the target observations, respectively.

SDSS ID (Abbr.)	z	A_r (mag)	SDSS r mag (mag)	$\log(L_{1.4GHz})$ (W Hz^{-1})	$\log(L_{[OIII]})$ (W)	$\log(M_*)$ (M$_\odot$)	Obs. date	Seeing FWHM (arcsec)
J072528.47+434332.4 (J0725)	0.069	0.25	16.37	23.06	33.90	10.9	2017-03-29	1.30
J075756.72+395936.1 (J0757)	0.066	0.14	15.36	23.98	34.12	10.8	2017-03-28	1.31
J081040.29+481233.1 (J0810)	0.077	0.14	15.87	23.70	33.54	10.9	2017-03-28	1.34
J082717.80+125430.0 (J0827)	0.065	0.10	16.00	22.71	33.36	10.7	2017-03-30	1.38
J083637.83+440109.5 (J0836)	0.055	0.08	15.25	23.94	33.79	11.1	2017-03-28	1.24
J083856.90+261037.5 (J0838)	0.051	0.14	16.41	22.62	33.57	10.3	2017-03-30	1.37
J090239.51+521114.7 (J0902)	0.098	0.05	15.50	23.94	33.25	11.4	2017-03-29	1.21
J091107.04+454322.6 (J0911)	0.098	0.05	17.33	22.62	33.26	10.7	2017-03-29	1.24
J093141.45+474209.0 (J0931)	0.049	0.04	17.07	22.54	33.38	10.0	2017-03-31	1.40
J095058.69+375758.8 (J0950)	0.041	0.05	15.29	23.37	33.26	10.8	2017-03-29	1.21
J103655.60+380321.4 (J1036)	0.051	0.06	14.45	22.82	33.79	11.2	2017-03-31	1.41
J110009.47+100312.1 (J1100)	0.064	0.08	17.24	22.85	32.98	10.2	2017-03-31	1.40
J110852.61+510225.6 (J1108)	0.070	0.04	15.89	23.07	33.84	11.0	2017-03-31	1.57
J114740.08+334720.4 (J1147)	0.031	0.05	14.29	22.52	33.94	10.7	2017-03-31	1.68
J115020.82+010423.1 (J1150)	0.078	0.07	17.70	22.97	33.29	10.7	2017-03-30	1.94
J120611.42+350525.6 (J12061)	0.081	0.05	15.71	22.92	33.89	11.1	2017-03-30	1.40
J120640.31+104652.8 (J12064)	0.089	0.06	17.62	23.41	33.02	11.0	2017-03-28	1.24
J123641.09+403225.7 (J1236)	0.096	0.06	17.82	23.08	33.57	10.5	2017-03-29	1.14
J124322.55+373858.0 (J1243)	0.086	0.05	15.69	23.35	33.97	11.2	2017-03-28	1.14
J125739.56+510351.4 (J1257)	0.097	0.03	16.34	23.20	33.33	11.1	2017-03-29	1.14
J132450.59+175815.0 (J1324)	0.086	0.06	16.67	23.35	33.36	10.7	2017-03-28	1.07
J135152.97+465026.1 (J1351)	0.096	0.04	17.04	23.26	33.21	10.6	2017-03-28	1.08
J135817.73+171236.7 (J1358)	0.095	0.10	16.87	23.21	33.93	10.9	2017-03-28	1.27
J141217.69+242735.9 (J1412)	0.069	0.06	15.42	23.19	33.79	11.1	2017-03-29	1.67
J152948.01+025536.7 (J1529)	0.077	0.13	16.56	22.93	33.21	10.8	2017-03-30	1.54
J155511.00+270056.2 (J1555)	0.083	0.12	17.36	22.92	33.47	10.4	2017-03-31	2.05
J160110.88+431138.1 (J1601)	0.072	0.04	17.09	22.99	34.24	10.4	2017-03-31	1.41
J160953.46+133147.8 (J1609)	0.036	0.11	15.06	23.01	32.86	10.8	2017-03-31	1.60
J162237.28+075349.5 (J1622)	0.088	0.22	17.10	23.19	33.77	10.6	2017-03-29	1.40
J163045.51+125752.7 (J1630)	0.065	0.15	16.93	22.78	33.89	10.1	2017-03-31	2.02

using four pointing offsets of 30 arcsec. Flat-field and image defect corrections are also improved by this process.

2.3   Reduction

The subsequent image processing, from initial reduction to construction of the final mosaic images, was done using THELI (Schirmer 2013). Bias corrections for each observation were performed via the subtraction of master bias frames, whilst master flat-field frames were used for flat-field corrections. These master frames were constructed by median-combining individual calibration frames that were taken on the same night as the given observation. The individual flat-

field images were dome flats with exposure times ~ 3s. Removal of the overscan level was performed on all calibration and science frames.

An astrometric solution for all calibrated images was calculated in THELI through cross-matching object catalogues produced for each image by SExtractor (Bertin & Arnouts 1996) with the all-sky USNO-B1 catalog (Monet et al. 2003). The comparison of these catalogues and the generation of the astrometric solution was performed within THELI using the Scamp pipeline for astrometry and photometry (see Bertin 2006). Cross-matching was only carried out for sources with apparent magnitudes ≤ 20 to prevent the astrometry from being overconstrained, whilst still provid-
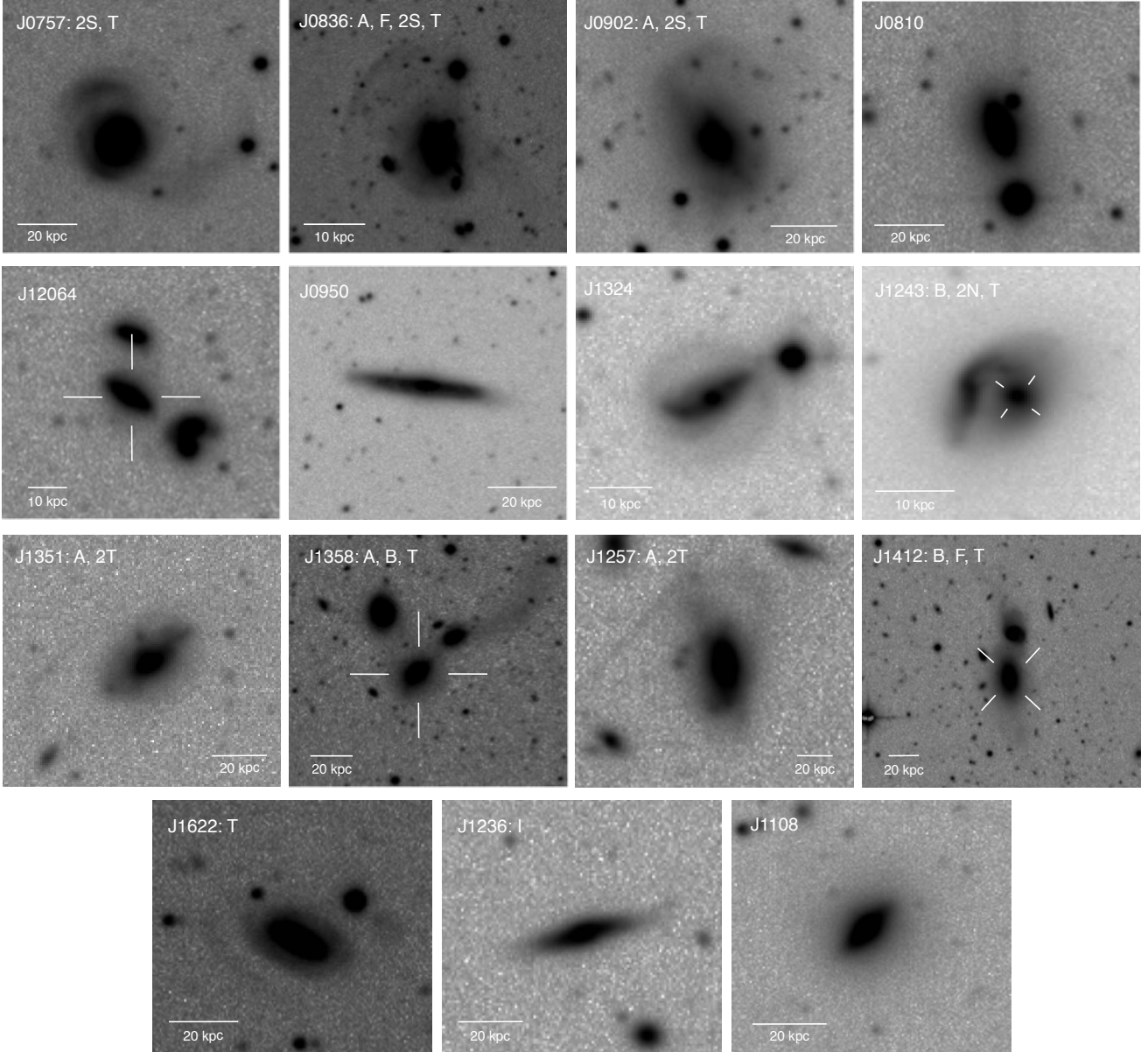
Figure 2. Deep *r*-band images of the half of the HERGs in the sample with the highest radio powers, lying within the range 23.06 < log(L$_{1.4\text{GHz}}$) < 24.0 W Hz^{-1}. The galaxies are also ordered in decreasing radio power from top-left to bottom-right within the figure. The images are centred on the targets and are identified within crosses on the images, where ambiguous. The abbreviated SDSS IDs are shown for each target, along with any interaction signatures from the classification scheme outlined in §3.1.1 that are associated with the hosts or companions clearly involved in the interactions. Approximate scale bars (in kpc) are displayed in all cases. The images are oriented such that north is up and east is left.

ing a sufficiently large number of objects to obtain a good solution.

To correct for variations in the sky background level across the images, THELI was used to produce a sky model and subtract it from the calibrated data. Prior to model creation, objects with a minimum of five connected pixels at a value of 1.5 σ above the measured background level were detected and removed using SExtractor. A sky model convolved with a Gaussian kernel with a FWHM of 60 pixels was found to produce the best results in almost all cases; the exception was J0902, for which a FWHM of 200 pix-

els was required due to a large gradient in the background level near a very bright foreground star. Coaddition of the four separate calibrated images was performed to produce the final mosaic image for each target, using the positional information from the prior astrometric solutions.

To calibrate the images photometrically, THELI was used to calculate photometric zero points for the coadded images of each of the targets. This was performed through comparison of the derived instrumental magnitudes for stars in the image field with their catalogued SDSS magnitudes. Only stars with instrumental magnitude errors ≤ 0.05 (as derived
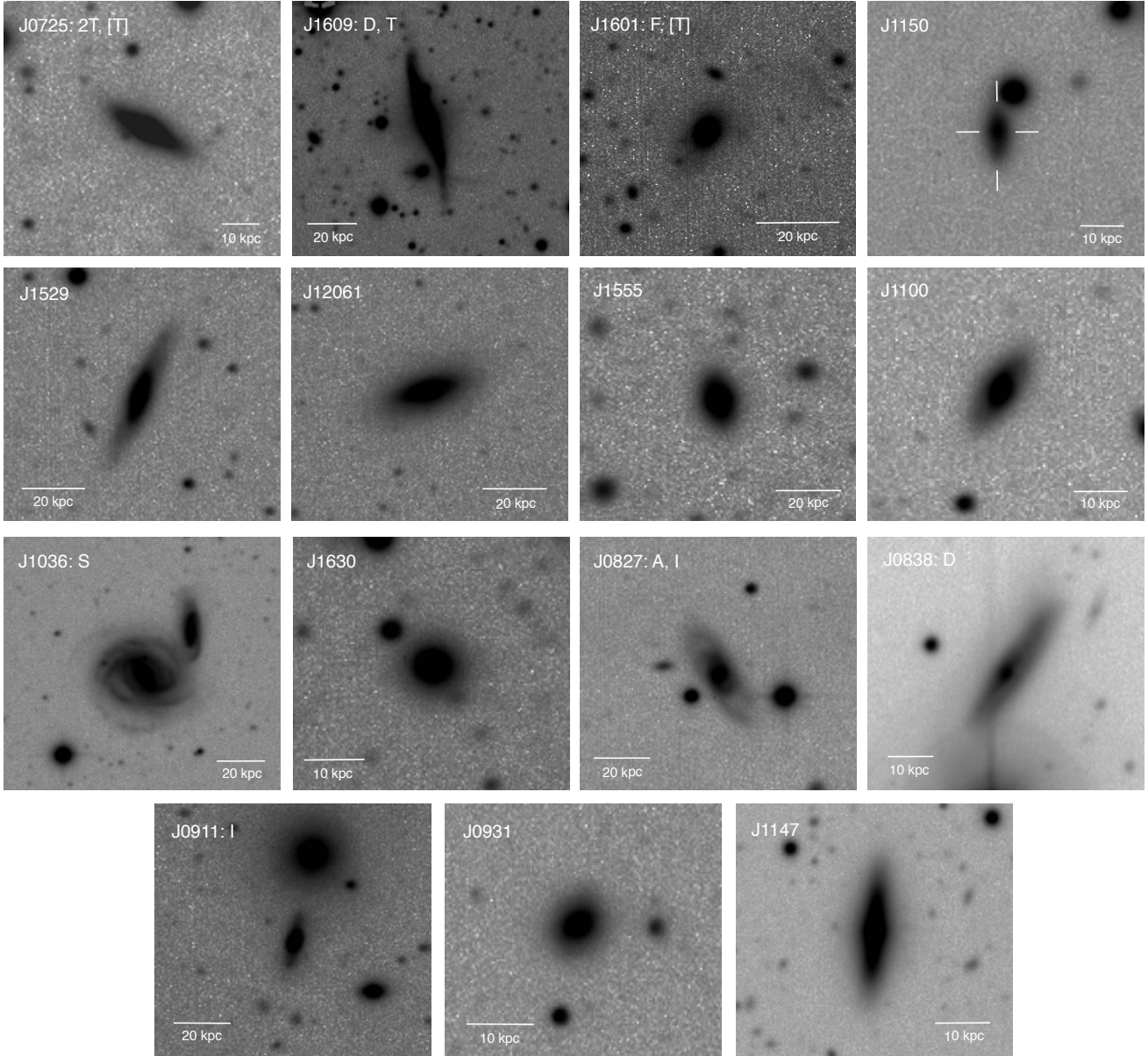
Figure 3. As Figure 2, but for the half of the HERGs in the sample with the lowest radio powers, lying within the range $22.5 < \log(L_{1.4GHz}) < 23.06$ W Hz^{-1}.

by `SExtractor`) and maximum counts ≤ 70 per cent of the saturation level were used for this process. This method has the advantage of automatically correcting for photometric variability throughout the nights, since the calibration stars are observed at the same time and at the same position on the sky as the galaxy targets. It also removes the reliance on average zero points derived from standard star observations.

3 DATA ANALYSIS AND RESULTS

Following the reduction outlined above (§2.3), the final coadded images were analysed to investigate the detailed optical morphologies of the AGN host galaxies in our radio-intermediate sample. The first goal of this was to identify and characterise any tidal features and other interaction signatures associated with the galaxies, in order to provide an indication of the importance of merger-based triggering of the nuclear activity (see §3.1). Following this, the morphological classes of the host galaxies were classified via both visual inspection (§3.2.1) and detailed modelling of their surface brightness profiles using the two-dimensional fitting algorithm `GALFIT` (Peng et al. 2002, 2010, see §3.2.2). Determining whether the population is primarily composed of early- or late-type galaxies provides an initial impression of how they compare to other radio galaxy samples, and is a factor that could be linked to the dominant triggering mechanism for the nuclear activity. The bulge-disk decomposition available from the `GALFIT` models also allows quantitative estimates of the level of disk- or bulge-dominance in the light

profiles to be made, assisting with the morphological classifications. The details of this data analysis are presented here.

3.1 Tidal features

3.1.1 Classification

Visual inspection of the images was performed by five human classifiers in order to identify any interaction signatures linked with the AGN host galaxies. To be consistent with the analysis performed for the deep images of the 2 Jy radio galaxies (Ramos Almeida et al. 2011, 2012, 2013), the classification scheme of Ramos Almeida et al. (2011) was used for this process. This scheme is adapted from that produced by Heckman et al. (1986) for their study of a selection of powerful radio galaxies, and is based on the morphological disturbances caused by tidal forces in the galaxy merger simulations of Toomre & Toomre (1972) and Quinn (1984). The tidal features and other interaction signatures are classified as follows:

(i) **Tail (T)** – a narrow curvilinear feature with roughly radial orientation;

(ii) **Fan (F)** – a structure similar to a tail, but that is shorter and broader;

(iii) **Shell (S)** – a curving filamentary structure with a roughly tangential orientation relative to a radial vector from the main body of the galaxy;

(iv) **Bridge (B)** – a feature that connects a radio galaxy with a companion;

(v) **Amorphous halo (A)** – the galaxy halo is misshapen in an unusual way in the image;

(vi) **Irregular (I)** – the galaxy is clearly disturbed, but not in a way that fits into any of the previous classifications;

(vii) **Multiple nuclei (e.g. 2N, 3N)** – two or more brightness peaks within a distance of 9.6 kpc;

(viii) **Dust lane (D)** – a clear linear dark structure within the galaxy.

A galaxy with a morphology that did not meet any of these criteria, or that only showed evidence of dust lanes (viii), was classified as undisturbed and hence non-interacting. Examples of each of the different classifications are indicated in Figures 2 and 3, which display the deep *r*-band images for the halves of the sample with highest and lowest radio powers, respectively – images within each Figure are also ordered by decreasing radio power from top-left to bottom-right.

Each classifier was provided with a FITS image of each of the radio galaxies in the sample and asked to identify and classify any interaction signatures that they believed to be associated with them. A brief description of their characteristics (e.g. orientation, extent, faintness) was also required to help avoid confusion when comparing classifications from different individuals. A qualitative estimate of the confidence of the classifications was also recorded by each assessor to aid with the process of combining results to produce final classifications. This method was carried out by each individual independently to avoid any influence from the results of others.

In order to avoid biases introduced by the galaxy properties, most importantly by their radio powers, only the cos-

Table 2. The number and corresponding proportion of galaxies deemed as having clear interaction signatures and no clear interaction signatures. For those with clear interaction signatures, specific proportions for each of the classifications outlined in §3.1.1 are also presented, in order of decreasing frequency. Only one occurrence of a certain classification of signature is considered for each galaxy, but each different classification is considered individually. The listed uncertainties are standard binomial errors.

Classification	Number of galaxies	Proportion of sample
Clear interaction signatures	16	53 ± 9 %
No clear interaction signatures	14	47 ± 9 %
Tidal tail (T)	12	40 ± 9 %
Amorphous halo (A)	6	20 ± 7 %
Shell (S)	4	13 ± 6 %
Irregular (I)	3	10 ± 5 %
Fan (F)	3	10 ± 5 %
Bridge (B)	2	7 ± 5 %
Dust lane (D)	2	7 ± 5 %
Double nucleus (2N)	1	3 ± 3 %

mological scale (kpc arcsec^{-1}) for each target was provided to each classifier prior to image inspection – this value was required to identify targets that host multiple nuclei. The independent results were combined by considering each individual classification as a 'vote', such that those voted for by the majority of the classifiers were considered in the final classifications for each target. Failing a favoured result, the noted certainty provided for each individual classification was considered. If no final decision had been made, the classifications were discussed by the assessors to gain an overall consensus. The final classifications for the interaction signatures associated with all galaxies in the sample are indicated in Table 3.

3.1.2 Proportions

Once the classification process had been carried out, the proportions of galaxies in the sample that showed signs of interaction were analysed. In an attempt to reduce ambiguity, the classified galaxies were separated into two categories: (i) 'clear interaction signatures' and (ii) 'no clear sign of interaction'. Category (i) only contained galaxies with interaction signatures that the assessors had deemed as certain following the visual classification process. The remaining galaxies, with indefinite or non-existent interaction signatures, were placed in category (ii). Due to the nature of this division, the number of galaxies that are classified as interacting can be considered to be a lower limit. Dust lanes (the D classification) were not considered to be a clear interaction signature. The proportion of galaxies in the sample that were placed in categories (i) and (ii) are presented in Table 2, along with the proportion that showed evidence for each individual type of interaction signature (i.e., T, F, S, B, A, I, 2N, D).

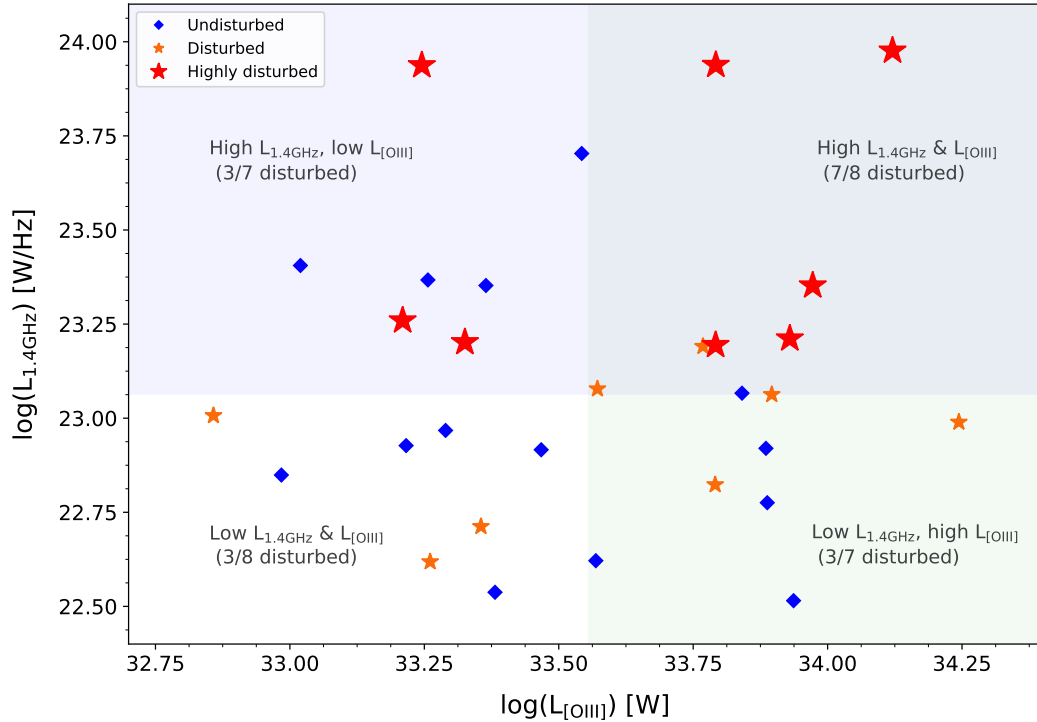Overall, 53 ± 9 per cent of the sample showed some sig-

Figure 4. A plot of the radio powers at 1.4 GHz against the [OIII] $\lambda5007$ luminosities for the galaxies in the sample. Galaxies with morphological signatures of disturbance are plotted as orange stars, and the larger red stars indicate those with high levels of disturbance. Undisturbed galaxies are plotted as blue diamonds. The blue shaded region indicates the half of the sample with the highest radio powers whilst the green-grey shaded region denotes the half with the highest [OIII] luminosities. The proportion of disturbed galaxies in each quadrant is indicated.

nature of a past or on-going interaction. When the sample is divided into two equally populated bins in radio power, it is found that galaxies in the most radio-powerful half of the sample $(23.06 < \log(L_{1.4GHz}) < 24.0 \text{ W Hz}^1)$ show interaction signatures more frequently than those in the least radio-powerful half $(22.5 < \log(L_{1.4GHz}) < 23.06 \text{ W Hz}^1)$ – 67 ± 12 per cent and 40 ± 13 per cent, respectively (see Figure 7). After conducting a two-proportion Z-test, it is found that the null hypothesis that these two proportions of interacting galaxies are the same can be rejected at a confidence level of 85.7 per cent $(1.5\,\sigma)$. However, given the proportions measured, it is found that a minimum of 63 galaxies would be needed in each half of the sample for the Z-test to reject the null hypothesis at the $3\,\sigma$ level, illustrating the need for more data. An improved statistical analysis will be performed in future papers in this series when further deep imaging data has been reduced and analysed.

Interestingly, the exact same proportions are found when dividing the sample into two equally populated bins in [OIII] $\lambda5007$ luminosity: 67 ± 12 per cent for the half with the highest luminosities $(33.56 < \log(L_{[OIII]}) < 34.24 \text{ W})$ and 40 ± 13 per cent for the half with the lowest luminosities $(32.86 < \log(L_{[OIII]}) < 33.56 \text{ W})$. Plotting $L_{1.4GHz}$ against $L_{[OIII]}$ for both the morphologically disturbed and undisturbed galaxies in the sample (Figure 4) reveals no significant correlation between the two parameters, however, as confirmed by a Pearson correlation test $(r = 0.077, p = 0.685)$. This is in line with what is seen at radio-intermediate powers in other studies (e.g. Best et al. 2005b). As such, $L_{1.4GHz}$ and $L_{[OIII]}$

are independent of one another within the sample, and, in fact, it can be seen in Figure 4 that the two sets of proportions are not provided by the same galaxies.

Following cursory visual inspection, however, eight of the galaxies in the sample show clear, highly disturbed morphologies or are involved in interactions with large-scale tidal tails, suggestive of major interactions: J0757, J0836, J0902, J1243, J1257, J1351, J1358 and J1412 (large red stars in Figure 4). All of these galaxies lie in the half of the sample with the highest radio powers, and hence none lie in the half with the lowest radio powers. Using a two-proportion Z-test, it is found that the null hypothesis that the proportion of highly disturbed galaxies in these two halves of the sample are the same can be rejected at a confidence level of 99.9 per cent $(3.3\,\sigma)$. We note that given that there were only eight of such galaxies in the entire sample, a more significant result could not have been observed.

Only 5 out of these 8 galaxies lie in the half with the highest [OIII] $\lambda5007$ luminosities, however, with the remaining 3 out of 8 seen to be in the half with the lowest [OIII] $\lambda5007$ luminosities. In this case, a two-proportion Z-test reveals that the null hypothesis that these two proportions are the same can only be rejected at a confidence level of 59.1 per cent $(0.8\,\sigma)$. These results suggest that the highly disturbed galaxy morphologies are linked with the radio powers of the AGNs, but are unlikely to be linked with their [OIII] $\lambda5007$ luminosities. We reserve further discussion on this matter for §4.1.2.
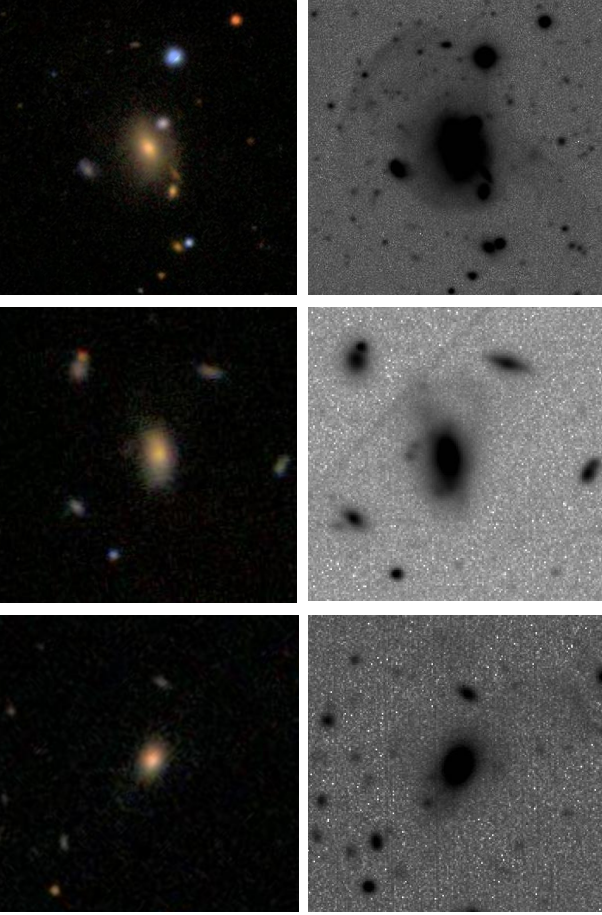
Figure 5. Example SDSS (left column; composite *g-r-i*) and INT/WFC (right column; *r*-band) images for three galaxies in the sample. The INT/WFC observations reveal interaction signatures that are not visible in the SDSS imaging, highlighting the importance of deep imaging observations for the detection of low surface brightness tidal features.

3.1.3 Surface brightness

To determine the surface brightness sensitivity achieved by the observations, as is important for comparison with other studies, surface brightness limits were calculated for the final coadded images. As outlined by Duc et al. (2015), determinations of surface brightness limits in deep imaging programs often vary, making effective comparisons difficult. Consequently, we clarify our technique here.

Our method is based on measuring the variations in the sky background level in the final coadded images, and closely follows that of Atkinson et al. (2013) for their analysis of faint tidal features in wide-field images from the Canada-France-Hawaii Telescope Legacy Survey (CFHTLS). We stress that the measurements were performed *after* all reduction, including the flattening achieved through the subtraction of a sky background model (see §2.3). The total counts were measured for 40 apertures of one-arcsecond in diameter for each of the final images. These were distributed in suitable locations − with minimal or no influence from the halos of bright objects − across the field of the CCD in which the targets were centred (WFC CCD4). The standard deviation in the sky background level within the apertures

(σ_{sky}) was then determined and converted to an apparent magnitude to provide final limiting surface brightness measurements. The mean σ_{sky} and $3\sigma_{\mathrm{sky}}$ limiting surface brightnesses over all observations are 28.0 mag arcsec^{-2} and 26.8 mag arcsec^{-2}, respectively. The measured standard deviation for these quantities is 0.3 mag arcsec^{-2}. σ_{sky} and $3\sigma_{\mathrm{sky}}$ limiting surface brightness magnitudes for all targets are presented in Table 3.

Following this, the surface brightness of each of the detected tidal features was determined. For consistency, these measurements were carried out using a similar method to that used for the limiting surface brightnesses, using the average counts measured in one-arcsecond apertures evenly distributed over the full extent of the tidal feature. In this case, however, matching background apertures were also placed in suitable locations surrounding the tidal feature. This allowed the measured count level to be corrected for background contributions arising from either residual sky background or underlying smooth galaxy emission.

The measured surface brightnesses of all visually-detected tidal features are listed along with their classifications in Table 3. The measurements were corrected for surface brightness dimming using values provided by the NASA/IPAC Extragalactic Database (NED), and for extragalactic extinction using the *r*-band extinction values listed in Table 1. Cosmological *K*-corrections were also applied following the redshift-colour method of Chilingarian et al. (2010), using the integrated *g-r* colours calculated from the available SDSS DR7 magnitudes. These corrections were performed to be consistent with those applied by Ramos Almeida et al. (2011) and ensure meaningful comparisons between the measured surface brightnesses of the two studies. The values calculated following all corrections are also presented in the table. Surface brightness measurements that are brighter than the σ_{sky} surface brightness limit for the target observation but fainter than the $3\sigma_{\mathrm{sky}}$ limit are considered as uncertain detections, and are included inside square brackets in the table. The tidal features that were confidently detected ranged in surface brightness from 20.6 mag arcsec^{-2} to 27.0 mag arcsec^{-2}, with a median of 25.4 mag arcsec^{-2}. The standard deviation of these measurements is 1.6 mag arcsec^{-2}.

Due mainly to degeneracies in galaxy merger model parameters (e.g. age, mass ratio, impact angle), it is currently difficult to determine physically meaningful properties from the exact measured surface brightnesses of tidal features. As a result, no detailed conclusions are drawn from the values are reported here, although the values are useful in a relative sense for comparing between different studies and samples. For instance, here we note that ~ 40 per cent of the tidal features that we detect are fainter than the limiting surface brightness of standard depth SDSS images (~ 25 mag arcsec^{-2}; Driver et al. 2016), highlighting the importance of the improved depth provided by the targeted observations. This can be seen clearly for the examples shown in Figure 5, where the INT/WFC observations reveal interaction signatures that are not detected in SDSS images.

Table 3. Surface brightness information for the targets in the sample. Column 1 displays the target names, which are the abbreviated forms of their SDSS IDs, as in Table 1. Column 2 denotes the level of surface brightness dimming in magnitudes per unit area as provided by the NASA/IPAC Extragalactic Database (NED). Columns 3 and 4 give the classification and measured surface brightness for the tidal features associated with each target. Column 5 shows these surface brightnesses after corrections for surface brightness dimming and foreground galactic extinction (A_r in Table 1), and cosmological K-correction following Chilingarian et al. (2010, online calculator available at http://kcor.sai.msu.ru/). The surface brightness limits derived from $\sigma_{\rm sky}$ and $3\sigma_{\rm sky}$, as per §3.1.3 are provided in Columns 6 and 7, respectively. All surface brightness measurements are in mag arcsec^{-2}. The values associated with tidal features with measured surface brightnesses fainter than the $3\sigma_{\rm sky}$ surface brightness limit but brighter than the $\sigma_{\rm sky}$ limit are indicated in square brackets.

Target	Dimming	Morphology	$\mu_{\rm AB}$ (mag arcsec^{-2})	$\mu_{\rm AB}^{\rm corr}$ (mag arcsec^{-2})	$\mu_{\rm AB}^{\sigma_{\rm sky}}$ (mag arcsec^{-2})	$\mu_{\rm AB}^{3\sigma_{\rm sky}}$ (mag arcsec^{-2})
J0725	0.292	2T, [T]	26.10, 26.50, [26.85]	25.49, 25.88, [26.24]	27.83	26.63
J0757	0.279	2S, T	23.23, 23.56, 25.41	22.75, 23.08, 24.93	27.99	26.80
J0810	0.326	-	-	-	28.39	27.20
J0827	0.279	A, I	-	-	27.40	26.21
J0836	0.237	A, F, 2S, T	22.64, 25.25, 26.08, 26.36	22.28, 24.89, 25.71, 25.99	28.28	27.09
J0838	0.220	D	-	-	27.93	26.74
J0902	0.409	A, 2S, T	23.47, 26.38, 23.60	22.92, 25.83, 23.05	28.20	27.00
J0911	0.409	I	-	-	27.89	26.70
J0931	0.209	-	-	-	28.16	26.97
J0950	0.176	-	-	-	28.00	26.81
J1036	0.218	S	25.10	24.78	28.23	27.03
J1100	0.274	-	-	-	27.97	26.77
J1108	0.295	-	-	-	27.99	26.80
J1147	0.136	-	-	-	28.27	27.08
J1150	0.332	-	-	-	27.41	26.21
J12061	0.341	-	-	-	27.20	26.01
J12064	0.376	-	-	-	28.18	26.98
J1236	0.401	I	-	-	28.09	26.89
J1243	0.361	B, 2N, T	20.62, 21.66	20.12, 21.66	27.72	26.53
J1257	0.402	A, 2T	24.81, 25.97	24.30, 25.46	27.83	26.64
J1324	0.362	-	-	-	27.89	26.69
J1351	0.402	A, 2T	23.15, 26.50	22.64, 25.98	28.25	27.06
J1358	0.399	A, B, T	25.43, 26.47	24.84, 25.88	28.12	26.92
J1412	0.293	B, F, T	24.12, 24.23, 25.63	23.69, 23.80, 25.21	28.07	26.88
J1529	0.322	-	-	-	27.78	26.59
J1555	0.346	-	-	-	28.12	26.93
J1601	0.301	F, [T]	25.08, [26.96]	24.68, [26.56]	28.09	26.90
J1609	0.152	D, T	26.17	25.88	27.99	26.80
J1622	0.367	T	26.51	25.84	28.05	26.86
J1630	0.273	-	-	-	28.14	26.95

3.2 Host morphologies

3.2.1 Visual inspection

When carrying out the visual inspection process outlined in §3.1.1, the classifiers were also asked to provide comments on the general morphological properties of the host galaxies. This was primarily done to provide an impression of their morphological types. For late-type galaxies, however, assessors also noted the level of disk warping and the rough disk orientation (from edge-on to face-on), which could assist with the interpretation of the interaction signature classifications. Late-type galaxies were those seen to have a significant disk or spiral-like morphology (discarding lenticular galaxies), and were found to be the most popular category

within the sample (43 per cent; 13/30). Early-type galaxies, appearing as elliptical-like or lenticular, were found to comprise 37 per cent (11/30) of the population, whilst the remaining 20 per cent (6/30) were judged to have morphologies too disturbed to classify – the 'merger' class. The visual classifications for all the galaxies in the sample are presented in the last column of Table 4.

Classifications based on visual inspection are also available for our sample in the public data release for the Galaxy Zoo project (Lintott et al. 2008, 2011). The project required participants to classify galaxies in composite g-, r- and i-band images from SDSS into one of the following categories: "Elliptical (E)", "ClockWise spirals (CW)", "Anti-ClockWise spirals (ACW)", "Edge-on spirals (Edge)", "Don't

Know (DK)" or "Merger (MG)". The vote fractions provided for the E classification are taken to indicate the likelihood of a galaxy being of early-type, whereas the sum of the vote fractions for the CW, ACW and Edge classifications ("Combined Spiral", CS) are taken as the likelihood of a galaxy being of late-type.

In our case, we only accepted a classification if the value of the lower error boundary on the vote fraction for the most popular category was greater than the value of the upper error boundary on the least popular category. In other words, the lower error boundary on the early-type vote fraction was required to be greater than the upper error boundary on the late-type vote fraction for a galaxy to be classed as early-type, and vice versa. The error boundaries considered for the vote fractions were 95 per cent confidence intervals. The vote fraction of the most popular classification was also required to be greater than 0.5 to ensure that the other two categories (DK and MG) were not favoured. Should these conditions not be met, the galaxy morphology was classed as uncertain. From this, it is found that 30 per cent of the sample (9/30) are classed as early-types, 37 per cent (13/30) as late-types, and the remaining 33 per cent (10/30) as uncertain.

As part of the Galaxy Zoo project, an attempt was also made to correct for biases introduced by the magnitude limit of SDSS and varying galaxy appearance with redshift – for details, see Bamford et al. (2009) and Lintott et al. (2011). 'Debiased' vote fractions are available for 28 of the galaxies in the sample, and when these results are considered, it is found that 25 per cent (7/28) are classed as early-types, 43 per cent (12/28) as late-types and the remaining 32 per cent (9/28) as uncertain. Since the biases tend to lead to overestimates of the number of early-type galaxies relative to late-types, debiasing of the vote fractions tends to increase the vote fractions for late-type galaxies relative to early-types on the whole, as is reflected here. The visual classification results from both the authors and the Galaxy Zoo project are summarised in Table 5 and discussed in §4.2.

3.2.2 Light profile modelling

More quantitative characterisation of the light distributions of the host galaxies was performed using the two-dimensional fitting algorithm GALFIT (Peng et al. 2002, 2010), which allows for the fitting of multiple structural components to galaxy light profiles. Our main motivation for doing this was to better identify the morphological types of the host galaxies (i.e. early-type vs. late-type), and to assess the relative contributions of bulge and disk light. In addition, the residual images generated as part of this process were also useful for clarifying any interaction signatures associated with the host galaxies. A well-defined procedure was followed to improve the consistency of the fitting process, starting with models of minimal complexity and only moving towards more complicated models if completely necessary.

In much of the previous literature, galaxy light distributions have been modelled using Sérsic profiles, and hence we chose to adopt this method during our modelling to allow for direct comparison to previous work. In GALFIT, the

Sérsic profile is described by

$$\Sigma(r) = \Sigma_e \exp\left\{-\kappa \left(\frac{\mathrm{r}}{\mathrm{r_e}}\right)^{\frac{1}{\mathrm{n}}} - 1\right\},$$

where $\Sigma(r)$ is the pixel surface brightness of the galaxy light at radius r, $\Sigma(r_e)$ is the value at r_e, the effective radius of the light profile, n is the Sérsic index, and κ is a constant coupled to n (Peng et al. 2002, 2010).

Traditionally, Sérsic profiles with indices around $n = 1$ (exponential) have been found to provide good fits for galaxy disks, and those with $n = 4$ (de Vaucouleurs) for galaxy spheroids (galaxy bulges and elliptical galaxies). Galaxies that appear to show both disk-like and bulge-like components have then been modelled with a combination of these two types of profile, in an attempt to separate the light profile characteristics for bulge-disk decomposition. Detailed bulge-disk decomposition of very nearby disk galaxies with various Hubble types (from S0 to Sc), however, suggests that classical-bulge-like components can have Sérsic indices as low as $n \sim 1.5 - 2$ at very high resolutions (Gao & Ho 2017). In an attempt to be as inclusive as possible whilst still separating disk-like and classical-bulge-like components clearly, we chose to constrain the Sérsic indices for disk-like and classical-bulge-like components to the following ranges: $n = 0.5$ to 1.5 for disk-like (late-type) components; and $n = 2$ to 5 for galaxy spheroid (early-type) components. As well as better distinguishing between disk-like and bulge-like components for determining the overall morphological class of the galaxy, this also had the advantage of minimising the effect of degeneracies in the models.

In addition to the Sérsic profiles, GALFIT also requires a representation of the point spread function (PSF) in the form of a FITS image. All modelling profiles are convolved with the PSF to account for the quality of the observational data. In some cases, an individual PSF component was also required in the models to account for strong, unresolved AGN emission at the centre of the galaxies. All PSFs were generated using the average light profile of non-saturated stars in the final coadded images for each of the targets. Two-dimensional surface profile plots of the light from these stars were visually inspected to ensure that they provided an adequate representation of the PSF at good signal-to-noise, considering both the measured seeing of the observations and the characteristic shape of the response from the CCDs. Following this, PSFs could be used in combination with Sérsic profiles for the modelling process.

The procedure used for the fitting involved multiple stages and terminated as soon as a suitable model was obtained. All of our models were produced using at least one Sérsic profile and used up to a maximum of three Sérsic profiles to avoid unwarranted complexity in the fitting process. Neighbouring stars and galaxies were modelled simultaneously with the targets to minimise their effect on accurately modelling the host galaxy light profiles. In all cases, pixels above 70 per cent of the saturation level were masked prior to fitting to avoid any issues introduced by the CCD response close to saturation. The process is outlined here:

(i) **Single Sérsic profile** – Initially, an attempt was made at fitting a single Sérsic profile, with a Sérsic index constrained to the ranges outlined above for each 'disk-like' and 'bulge-like' profiles. Determining which of the two pro-

Table 4. The results from detailed modelling of the host galaxy light profiles using `GALFIT`. The abbreviated target names are shown in Column 1, as listed in Table 1. For each model component, Columns 2-6 provide: (2) the component type (i.e. Sérsic or PSF) and its classification as bulge-like (B), disk-like (D) or intermediate (I) for multi-component fits; (3) the Sérsic index; (4) the effective radius in kpc; (5) the axis ratio; (6) the derived apparent magnitude. Columns 7-10 then present information derived from the overall models (combination of all components): (7) total apparent magnitude; (8) ratio of bulge-to-disk light (where relevant); (9) ratio of bulge-to-total light; (10) ratio of disk-to-total light. The morphological types from the visual inspection performed by the authors are also presented in Column 11, with their classifications as either mergers or early- (E) or late-type (L) galaxies indicated in brackets.

Target	Comp. Type	n	R_e (kpc)	b/a	m_c	m_t	B/D	B/T	D/T	Visual class.
(1)	(2)	(3)	(4)	(5)	(6)	(7)	(8)	(9)	(10)	(11)
J0725	Sérsic (B)	2.00	0.78	0.67	17.94	16.75	0.50	0.33	0.67	Lenticular (E)
	Sérsic (D)	0.92	5.06	0.22	17.19					
J0757	-	-	-	-	-	-	-	-	-	Merger
J0810	-	-	-	-	-	-	-	-	-	Lenticular (E)
J0827	Sérsic (B)	2.00	1.42	0.58	17.73	16.35	0.39	0.28	0.72	Spiral (L)
	Sérsic (D)	0.75	6.16	0.46	16.70					
J0836	Sérsic	5.00	6.70	0.64	15.08	15.08	-	-	-	Merger
J0838	Sérsic (B)	3.29	4.02	0.35	16.08	15.20	0.79	0.44	0.56	Edge-on disk (L)
	Sérsic (D)	0.50	9.67	0.22	15.83					
J0902	Sérsic	5.00	14.42	0.70	15.23	15.23	-	-	-	Merger
J0911	Sérsic (I)	2.00	1.74	0.46	18.38	17.52	-	-	-	Spiral (L)
	Sérsic (I)	1.50	6.79	0.25	18.21					
	PSF	-	-	-	21.91					
J0931	Sérsic	3.13	0.55	0.36	17.82	17.02	-	-	-	Elliptical (E)
	Sérsic	2.00	2.55	0.89	17.72					
J0950	Sérsic (B)	2.54	6.74	0.23	15.78	15.12	1.21	0.55	0.45	Edge-on disk (L)
	Sérsic (D)	0.50	14.06	0.11	15.99					
J1036	Sérsic (B)	5.00	6.22	0.54	14.94	14.36	1.41	0.59	0.41	Spiral (L)
	Sérsic (D)	0.50	12.63	0.76	15.31					
J1100	Sérsic (B)	2.00	1.38	0.34	17.89	17.41	1.80	0.64	0.36	Spiral (L)
	Sérsic (D)	0.52	4.49	0.39	18.53					
J1108	Sérsic (B)	2.00	1.50	0.74	16.65	15.87	1.48	0.60	0.40	Lenticular (E)
	Sérsic (D)	1.36	4.86	0.20	16.86					
	PSF (B)	-	-	-	18.28					
J1147	-	-	-	-	-	-	-	-	-	Lenticular (E)
J1150	Sérsic (B)	2.11	2.64	0.52	18.51	17.69	0.89	0.47	0.53	Spiral (L)
	Sérsic (D)	0.50	4.08	0.20	18.38					
J12061	Sérsic (B)	5.00	10.00	0.40	15.77	15.62	6.78	0.87	0.13	Lenticular (E)
	Sérsic (D)	0.96	5.75	0.20	17.85					
J12064	Sérsic (B)	5.00	5.82	0.62	17.78	17.35	2.04	0.67	0.33	Spiral (L)
	Sérsic (D)	0.50	4.49	0.18	18.55					
J1236	Sérsic (B)	2.00	1.33	0.62	19.74	17.88	0.22	0.18	0.82	Edge-on disk (L)
	Sérsic (D)	0.61	6.29	0.16	18.09					
J1243	-	-	-	-	-	-	-	-	-	Merger
J1257	-	-	-	-	-	-	-	-	-	Merger
J1324	-	-	-	-	-	-	-	-	-	Spiral (L)
J1351	-	-	-	-	-	-	-	-	-	Merger
J1358	Sérsic	3.79	1.63	0.27	18.71	16.96	-	-	-	Elliptical (E)
	Sérsic	2.91	5.11	0.61	17.20					
J1412	Sérsic	4.79	2.56	0.56	16.18	15.38	-	-	-	Elliptical (E)
	Sérsic	2.00	9.66	0.62	16.08					
J1529	Sérsic (B)	5.00	2.78	0.70	18.05	16.56	0.34	0.25	0.75	Edge-on disk (L)
	Sérsic (D)	0.50	5.63	0.19	17.84					
	Sérsic (D)	0.82	10.78	0.18	17.46					

Table 4 – *continued*

Target	Comp. Type	n	R_e (kpc)	b/a	m_c	m_t	B/D	B/T	D/T	Visual class.
(1)	(2)	(3)	(4)	(5)	(6)	(7)	(8)	(9)	(10)	(11)
J1555	Sérsic (B)	4.16	1.39	0.51	17.99	17.51	1.79	0.64	0.36	Lenticular (E)
	Sérsic (D)	0.50	4.49	0.39	18.62					
J1601	Sérsic	4.44	1.59	0.62	17.07	17.07	-	-	-	Elliptical (E)
J1609	Sérsic (B)	2.00	4.00	0.77	16.37	15.09	0.59	0.31	0.69	Edge-on disk (L)
	Sérsic (D)	1.50	3.97	0.04	17.00					
	Sérsic (D)	0.50	9.87	0.13	15.79					
J1622	Sérsic (D)	0.50	4.64	0.30	17.81	17.23	0.09	0.09	0.91	Spiral (L)
	Sérsic (D)	0.50	9.33	0.54	18.42					
	PSF (B)	-	-	-	19.90					
J1630	Sérsic	4.10	1.63	0.88	16.93	16.93	-	-	-	Elliptical (E)

files provided the best fit gave a first impression of the morphological class of the host galaxy. It was found that this stage alone generated a sufficient model for 4 out of the 30 galaxies (13 per cent), with no additional component required.

(ii) **Two Sérsic profiles** – Failing success after stage (i), an attempt was made at fitting a model with two constrained Sérsic components, in the order: 1) one disk-like profile and one bulge-like profile (bulge-disk decomposition); 2) two disk-like or two bulge-like profiles (two-component late-type or early-type). This combination proved sufficient for 14 out of the 30 galaxies (47 per cent), and provided the majority of successful models.

(iii) **Two Sérsic profiles + PSF** – For 3 of the 30 galaxies (10 per cent), a PSF component was required in addition to the two Sérsic profiles to model strong, unresolved AGN emission. The PSF components were only accepted after the presence of strong emission lines had been confirmed from inspection of the SDSS spectrum.

(iv) **Three Sérsic profiles** – The most complex cases required a model with three constrained Sérsic components to produce a suitable fit. These were all decomposed into disk-like and bulge-like components, either as two disk-like profiles and one bulge-like profile, or two bulge-like profiles and one disk-like profile. This was necessary for 2 of the 30 galaxies (7 per cent). If a good fit was still not obtainable at this point, the fitting process was terminated to avoid unwarranted complexity in the models.

In total, the overall light profiles of 23 (77 per cent) of the host galaxies were deemed to be recovered with reasonable accuracy using this process. The majority of models for the remaining seven objects failed due to issues related to the highly disturbed nature of the galaxy morphologies due to mergers (J0757, J1243, J1257, J1351). The unusual morphology of J1324 meant that a suitable fit could not be obtained before the models became too complex – it is possible that this target has also been disturbed by an interaction, though the authors did not deem this clear enough for the galaxy to be classified as such. In the case of J0810, the presence of a nearby bright star caused any modelling attempts

to produce an inaccurate representation of the galaxy light profile. Finally, a large proportion of the inner regions of the galaxy J1147 was saturated in the exposures, so any model fitting to this galaxy was deemed unreliable.

In cases that required at least two Sérsic profiles for accurate modelling, the morphology and model parameters for the sub-components were inspected to search for distinct bulge-like and disk-like components. For J0911, the model components cannot be separated in this way. In this case, both components have Sérsic indices that lie in the range $n = 1 - 2$, and their two-dimensional morphologies are intermediate between those of bulges and disks. Such components have been identified in previous studies (Floyd et al. 2004; Inskip et al. 2010; Falomo et al. 2014; Urbano-Mayorgas et al. 2019), and we refer to these as 'intermediate' (I) components. We also note that J1036 shows a highly detailed spiral arm, bulge and bar structure, along with signatures of past or on-going interactions. Detailed fitting of these structures was not performed, and, as such, the accuracy of the model for this galaxy is reduced compared to the others.

The key parameters for each of the individual components of the GALFIT models are presented in Table 4. Where appropriate, the derived bulge-to-disk light ratios (B/D) and their respective contributions to the total light profile (B/T and D/T) are reported. These ratios were not calculated for models that produced good fits to the overall light profile but did not separate into bulge-like and disk-like components. It is found that the majority (8 out of 15) of galaxies for which both bulge and disk components were required were disk-dominated, having a median bulge-to-disk ratio of B/D ~ 0.8. All four single Sérsic models and three two Sérsic models (one also with a PSF component) required only early-type profiles. When added to the bulge-dominated galaxies, it is hence found that 14 out of the 23 galaxies that could be modelled (61 per cent) have early-type profiles, with 8 out of 23 (35 per cent) having late-type profiles (disk-dominated) and 1 out of 23 (4 per cent) having an intermediate profile.

Given that there is a mixture of morphological types found within the sample, it is also interesting to determine
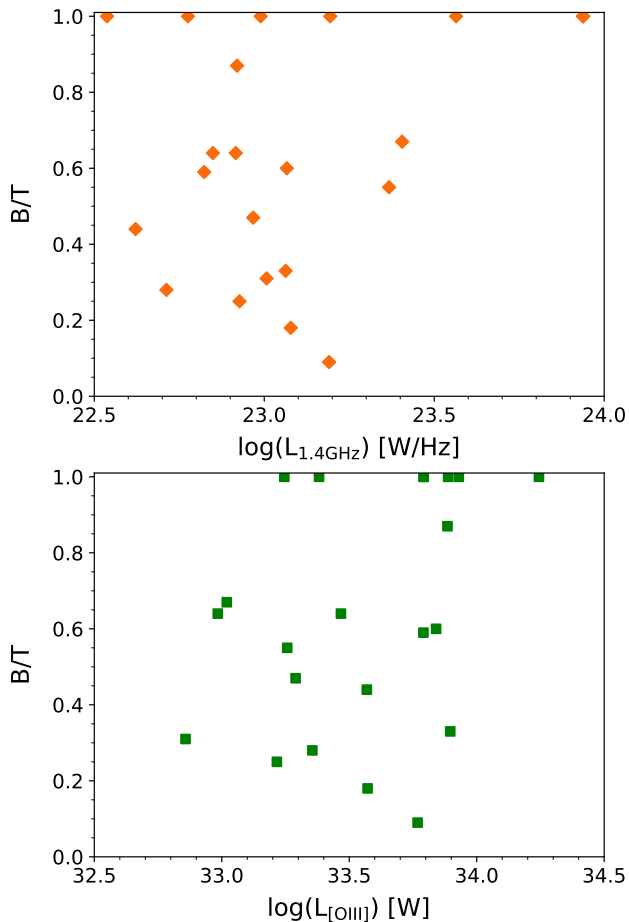
Figure 6. The fraction of the total light represented by the bulge-like components in the GALFIT models (B/T) against the radio powers (upper panel) and [OIII] $\lambda5007$ luminosites (lower panel) of the sources. All galaxies with successful models are included, excluding the galaxy that has only intermediate components (J0911). Galaxies with light profiles represented by only early-type components are considered to have B/T = 1.

whether there is any relationship between the level of bulge-dominance in the galaxy light profiles and the AGN radio or optical luminosity. Figure 6 shows the fraction of light contributed by the bulge-like components of the GALFIT models against both $L_{1.4\mathrm{GHz}}$ and $L_{[\mathrm{OIII}]}$ for all galaxies that were modelled successfully – this excludes J0911, which has only intermediate components. Here, galaxies with only early-type components in their models are considered as having all of their light contributed by a bulge component. From this, it is clear that there is no trend in the bulge-dominance of the galaxy light with either $L_{1.4\mathrm{GHz}}$ or $L_{[\mathrm{OIII}]}$, as confirmed by Pearson correlation tests ($r = 0.301$, $p = 0.173$ and $r = 0.338$, $p = 0.124$, respectively). This suggests that although the radio-intermediate HERGs represent a greatly changed population of morphological types to their predominantly giant elliptical counterparts at high radio powers, the galaxy morphologies do not change gradually with the radio or optical luminosity of the AGN. Rather, there is a mix of morphological types at all optical/radio luminosities in the radio-intermediate range.

4 DISCUSSION

Our analysis of deep *r*-band images of 30 local radio-intermediate HERGs has allowed us to characterise their detailed optical morphologies, including both signatures of past or on-going interactions and their overall morphological types. In §3.1.2, we showed that 53 ± 9 per cent of the sample show interaction signatures, with the proportions within the most radio-powerful and least radio-powerful halves of the sample being 67 ± 12 per cent and 40 ± 13 per cent, respectively. These exact same proportions are found for the respective halves of the sample with the highest and lowest [OIII] luminosities. It is found, however, that all eight of the galaxies that show the highest levels of disturbance lie in the most radio-powerful half of the sample. This is not seen when the sample is divided in two by [OIII] luminosity, where 5 out of 8 these galaxies lie in the half of the sample with the highest [OIII] luminosities and 3 out of 8 in the half with the lowest [OIII] luminosities (see Figure 4).

Both visual inspection and in-depth modelling of the host galaxy light distributions has revealed a mixture of morphological types within the sample (§3.2.1 and §3.2.2), with half showing evidence of a significant disk-like contribution to the galaxy light profile: 8 are classified as late-type based on GALFIT models (disk-dominated) and 14 as early-type (bulge-dominated or elliptical). The remainder proved unsuitable for accurate bulge-disk decomposition, four because of very highly disturbed morphologies resulting from mergers or interactions. Through comparison with previous work on radio AGN triggering and host morphologies, the implications of these results are discussed in this section.

4.1 Triggering of the nuclear activity

4.1.1 Importance of galaxy mergers and interactions

The focus of previous studies of radio AGN triggering has primarily been the most radio-powerful AGNs (e.g. those in the 3CR and 2 Jy samples), most probably because these were the easiest objects to study when the field began to develop. As discussed in §1, radio AGNs with high-excitation emission spectra (HERGs or SLRGs), such as those considered here, are often linked with an accretion mode in which cold gas fuels the black hole through a geometrically thin, optically thick accretion disk (e.g. see Heckman & Best 2014). Study of exactly what would cause the radial inflow of gas towards the innermost regions to trigger the nuclear activity has produced mixed results, with possible mechanisms including the tidal torques introduced by galaxy mergers and interactions or the action of non-axisymmetric features in galaxy disks such as bars, oval distortions and spiral arms (e.g. Hopkins & Quataert 2010; Heckman & Best 2014).

To date, the most extensive deep imaging study for radio-powerful AGNs with high-excitation optical emission has been carried out by Ramos Almeida et al. (2011, 2012, 2013) for SLRGs in the 2 Jy sample ($0.05 < z < 0.7$), which provides strong evidence to suggest that major galaxy interactions could trigger the nuclear activity. Ramos Almeida et al. (2011) find that 94 ± 4 per cent of the SLRGs in their sample show high-surface brightness signatures of past or on-going interactions, corroborating prior suggestions that radio galaxies with strong optical emission have highly disturbed optical morphologies (Heckman et al. 1986; Smith &

Heckman 1989a,b). They also found that the rate of merger signatures was significantly higher than those found for control samples of elliptical galaxies in both the OBEY survey (Tal et al. 2009) and the Extended Groth Strip (EGS; Zhao et al. 2009) matched in luminosity and redshift, when the same surface brightness limits are considered (Ramos Almeida et al. 2012). In addition, Ramos Almeida et al. (2013) find the 2 Jy SLRGs to preferentially reside in group-like environments that are denser than those of the EGS control galaxies but less dense than the cluster-like environments of the WLRGs in the sample. Group-like environments are well-suited to galaxy mergers, having a relatively high galaxy density without the high velocity dispersions of clusters that can suppress galaxy mergers (Quinn 1984; Popesso & Biviano 2006).

In the upper panel of Figure 7, we plot the proportion of radio AGNs that show tidal features and other interaction signatures against radio power at 1.4 GHz ($L_{1.4GHz}$) for both our radio-intermediate HERGs and the SLRGs in the 2 Jy sample. Comparing the two samples in their entirety, the proportion of interacting galaxies in the radio-intermediate sample is found to be 53 ± 9 per cent (16/30), a difference at the $3.8\,\sigma$ level from that found for the SLRGs in the 2 Jy sample (94 ± 4 per cent; Ramos Almeida et al. 2011). Dividing our sample by radio power, it is also seen that disturbed galaxies are found more frequently in the most radio-powerful half (67 ± 12 per cent) of the sample than in the least radio-powerful half (40 ± 13 per cent) – a difference at the $1.5\,\sigma$ level. These results appear, therefore, to be consistent with a reduction in the proportion of radio AGNs with high-excitation optical emission lines that are triggered by galaxy interactions with decreasing radio power.

As shown in §3.1.2, however, the same proportions are found when the sample is divided into two equally populated bins in [OIII] $\lambda5007$ luminosity ($L_{[OIII]}$): 67 ± 12 per cent for the higher $L_{[OIII]}$ half and 40 ± 13 per cent for the lower $L_{[OIII]}$ half. The lack of correlation between $L_{1.4GHz}$ and $L_{[OIII]}$ for the galaxies in the sample also means that the galaxies giving the measured proportions in each case are, in fact, different (see Figure 4). In the lower panel of Figure 7, these proportions are again compared to those found for the 2 Jy SLRGs, but this time plotted against $L_{[OIII]}$. From this, we see that the results are also consistent with a reduction in the level of merger-based triggering with decreasing optical ($L_{[OIII]}$) power, often also considered to be a proxy for the bolometric luminosity of the AGN (e.g. Heckman et al. 2004).

A further point of interest comes from comparing the measured surface brightnesses for the interaction signatures in the two studies. Figure 8 shows the distribution of surface brightness measurements for the tidal features both from this work and Ramos Almeida et al. (2011), after accounting for surface brightness dimming, foreground galactic extinction and cosmological K-correction. Although both studies have comparable image depths, we see that the 2 Jy SLRGs typically show interaction signatures of higher surface brightness – the faintest securely detected features have (corrected) surface brightnesses of $\mu_r^{corr} = 25.88$ mag arcsec^{-2} (Ramos Almeida et al. 2011) and $\mu_r^{corr} = 25.99$ mag arcsec^{-2} (this work), but the median values are $\mu_r^{corr} = 23.44$ mag arcsec^{-2} and $\mu_r^{corr} = 24.84$ mag arcsec^{-2}, respectively. This suggests that the galaxy interactions that trigger
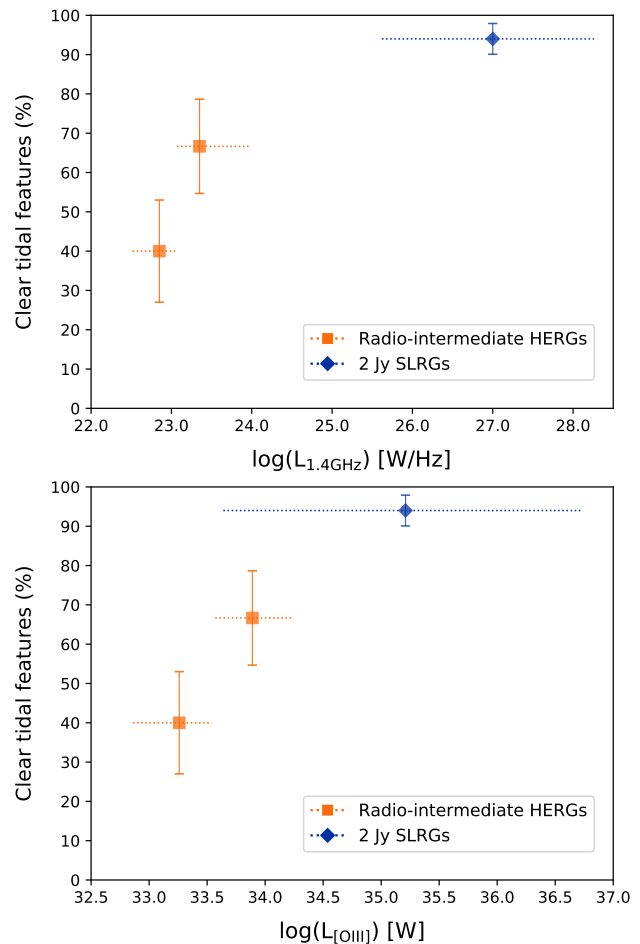

Figure 7. The percentage of HERGs in the current sample (orange squares) and SLRGs in the 2 Jy sample (blue diamonds; Ramos Almeida et al. 2011) that show clear tidal features, plotted against their radio powers at 1.4 GHz (top panel) and their [OIII] $\lambda5007$ luminosities (bottom panel). The results for each half of the radio-intermediate sample when split by their $L_{1.4GHz}$ or $L_{[OIII]}$ values are shown separately. The horizontal lines indicate the relevant $L_{1.4GHz}$ or $L_{[OIII]}$ ranges in each case, and the points represent their median values. Note that although the HERG and SLRG classifications are different, they are in broad agreement with one another.

the 2 Jy SLRGs are likely to be more major mergers than those that may trigger the radio-intermediate HERGs.

We note, however, that there are some caveats to consider when comparing our results with those of the 2 Jy studies. Firstly, it is seen that all the SLRGs in the 2 Jy sample for which stellar masses have been measured have values $\sim 10^{11}$ M$_\odot$ and above (Tadhunter 2016). This is above the median value for the radio-intermediate HERGs in the current sample ($10^{10.8}$ M$_\odot$), which can have stellar masses that are down to an order a magnitude lower ($\sim 10^{10}$ M$_\odot$). In addition, a mixture of early-type and late-type galaxies are seen in the radio-intermediate HERG population, whereas the vast majority of 2 Jy radio galaxies are associated with early-type morphologies. Finally, although there is a high degree of overlap between the HERG and SLRG classifications, the schemes are not equivalent (see Tadhunter 2016).
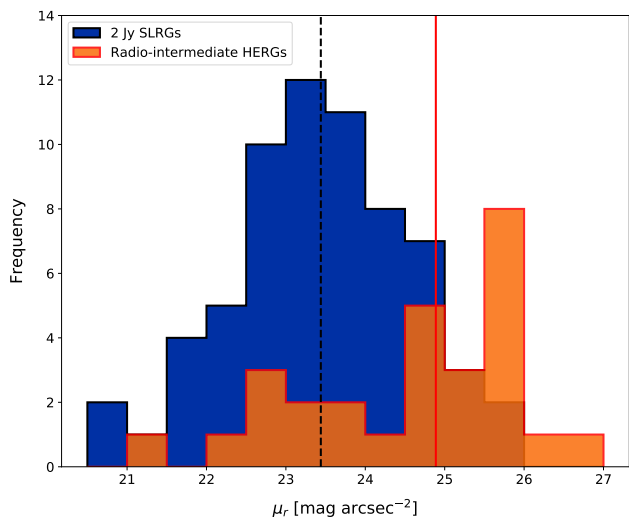
Figure 8. The distributions of tidal feature surface brightness measurements for the radio-intermediate HERGs (orange) and 2 Jy SLRGs (blue; Ramos Almeida et al. 2011). All values are in the AB system, and are corrected for surface brightness dimming, foreground galactic extinction and cosmological K-correction. The median values are indicated by the solid red line for the radio-intermediate HERGs and the dashed black line for the 2 Jy SLRGs.

4.1.2   Highly disturbed galaxies

The discussion in the previous section was based on the detection of *any* sign of morphological disturbance, regardless of the level. This includes objects for which the low-surface-brightness features are only visible after careful manipulation of the image contrast levels. However, for a subset of eight objects, the signs of galaxy interactions are obvious even on cursory inspection of the images. This subset of highly disturbed systems includes all six of the galaxies that the authors deemed too disturbed to classify accurately by visual inspection (J0757, J0836, J0902, J1243, J1257, J1351; the 'merger' class), four of which could also not be modelled with `GALFIT` on this basis (J0757, J1243, J1257, J1351). A further two galaxies are included based on the fact that they are strongly interacting with companion galaxies (J1358, J1412), as demonstrated by the presence of large-scale tidal features that provide an alternative indication of on-going major mergers (e.g. see Duc et al. 2015). In addition, it is seen that 6 out of 8 of these galaxies have at least one tidal feature at relatively high surface brightness ($\leq 24\,\mathrm{mag\,arcsec^{-2}}$), including all five galaxies with surface brightnesses greater than the median measured for the strongly disturbed 2 Jy SLRGs.

When the sample is divided in two by radio power, *all* of these eight highly disturbed systems are found to lie in the half of the sample with the highest radio powers. In contrast, they lie in both halves of the sample when divided by their [OIII] λ5007 luminosities. Comparing the proportions found in each of the two halves in both cases, a $3.3\,\sigma$ difference in proportions is found when dividing the sample by radio power, but only a $0.8\,\sigma$ difference when dividing by [OIII] λ5007 luminosity. We again note that given that there are only eight of these highly disturbed galaxies in

the entire sample, a more significant result could not have been observed when the division by radio power is made. Therefore, these resuts suggest that triggering through major galaxy interactions is linked with the radio powers of the HERGs, but not so strongly linked with their [OIII] λ5007 luminosities.

In combination with the results discussed in §4.1.1, this is therefore consistent with a picture in which the relative importance of mergers and interactions for triggering radio AGNs with HERG spectra is related to their radio powers. In line with the results of Ramos Almeida et al. (2011, 2012, 2013), mergers appear to be important for triggering those with higher radio powers, with all of the most highly disturbed galaxies in the radio-intermediate sample lying in the half with the highest radio powers, notably including the three most-radio powerful cases. This is aligned with a reduction in the proportion of radio-intermediate HERGs that show any sign of disturbance from the most radio-powerful half to the least-radio powerful half of the sample, suggesting that other triggering mechanisms must be important when moving towards lower radio powers.

4.2   Host morphologies

As mentioned in §1, powerful radio galaxies (typically $L_{1.4\mathrm{GHz}} > 10^{25}\,\mathrm{W\,Hz^{-1}}$) have long been associated with giant elliptical hosts (e.g. Matthews et al. 1964; Dunlop et al. 2003; Best et al. 2005b). There are, however, some suggestions that late-type hosts could be more common towards lower radio powers (Sadler et al. 2014; Tadhunter 2016). This could be particularly apparent for HERGs, if Seyfert galaxies are indeed considered as their low radio power equivalents. Crudely, one might therefore expect that radio-intermediate HERGs would manifest as a mixed population of galaxy morphologies, representing the transition from early-type galaxies at higher radio powers to late-type galaxies at lower radio powers.

Table 5 compares the morphological classifications of the galaxies in the sample as obtained from visual inspection, both from this work and the Galaxy Zoo project, and the detailed light profile modelling performed using `GALFIT` – the methods are described in §3.2.1 and §3.2.2, respectively. Regardless of the technique, it is immediately clear that there is no dominant class of host galaxy morphology, and that radio-intermediate HERGs do in fact represent a mixture of late-type and early-type morphologies. As discussed in §3.2.2, however, we can also rule out the idea that the host morphology – as quantified using the B/T ratio – changes gradually with radio or optical AGN luminosity along the HERG sequence.

Considering the results of the visual inspection, we see that the proportion of galaxies classified as late-type and early-type are consistent between this work and Galaxy Zoo project, with a slight preference for late-types relative to early-types. The main difference between the two lies in the higher proportion of hosts categorised as "Merger" or "Don't Know" in the Galaxy Zoo results compared to those classified to be merging by the authors. This is perhaps unsurprising given the relative inexperience of the participants in the project and the common occurrence of lenticular galaxies, which are hard to categorise in the Galaxy Zoo classification scheme.

Table 5. The number and corresponding proportion of galaxies in the sample with the indicated morphological classifications. The results from visual inspection, both in this work and from the Galaxy Zoo project (Lintott et al. 2008, 2011), and detailed light profile modelling using `GALFIT` (Peng et al. 2002, 2010) are presented. Note that debiased Galaxy Zoo results were only available for 28 of the galaxies, as indicated. The quoted uncertainties are standard binomial errors.

Visual inspection	Number	Prop.
Late-type (Spiral/disk)	13	43 ± 9 %
Early-type (Elliptical/Lenticular)	11	37 ± 9 %
Mergers	6	20 ± 7 %

Galaxy Zoo	Number	Prop.
Late-type (Spirals)	11	37 ± 9 %
Early-type (Ellipticals)	9	30 ± 8 %
Uncertain (Merger/"Don't Know")	10	33 ± 9 %

Galaxy Zoo – *debiased (28 only)*	Number	Prop.
Late-type (Spirals)	12	43 ± 9 %
Early-type (Ellipticals)	7	25 ± 8 %
Uncertain (Merger/"Don't Know")	9	32 ± 9 %

Light profile modelling	Number	Prop.
Late-type	8	27 ± 8 %
– one component	*0*	
– disk-dominated	*8*	
Early-type	14	47 ± 9 %
– one component	*7*	
– bulge-dominated	*7*	
Intermediate	1	3 ± 3 %
Undetermined	7	23 ± 8 %
– mergers (major disturbance)	*5*	*16 ± 7 %*
– fitting issues	*2*	*7 ± 5 %*

It is important to note, however, that visual classifications are always subject to biases (e.g. see Cabrera-Vives et al. 2018), which, despite attempts (e.g. Bamford et al. 2009; Willett et al. 2013), are difficult to correct for, especially for small sample sizes. This provided strong motivation for performing detailed modelling of the galaxy light profiles, with the goal of providing a more quantitative basis for the galaxy classifications. Interestingly, the proportion of early-type hosts relative to late-types is seen to be higher in this case, in contrast with the results of the visual inspections. It is worth noting, on the other hand, that a total of 15 out of the 30 galaxies in the sample required both bulge-like and disk-like components to fit their light profiles, a proportion comparable to the number classified as late-types from the visual classification. In addition, the majority of multi-component models were disk-dominated, as is evidenced by the median bulge-to-disk ratio of B/D ~ 0.8.

One further point of interest is that the presence of major disk components in the galaxy light profiles opens up the possibility of AGN triggering via secular mechanisms related to galaxy disks, as mentioned in §4.1. Disk instabilities have been suggested as an important alternative triggering mechanism for AGNs below quasar luminosities (e.g. Menci et al. 2014), although it is uncertain whether this would be important outside of the violent conditions expected in clumpy disk galaxies at higher redshifts (Bournaud et al. 2012). However, it is thought that the weaker and flatter bulges sometimes seen in late-type galaxies could be built up by instabilities in the disks (Kormendy & Kennicutt 2004), which could simultaneously trigger the nuclear activity. In addition, bar-driven fuelling could contribute in at least some cases (e.g. Galloway et al. 2015). Given the reduced proportion of interacting galaxies and increased proportion of late-type hosts that are found in the sample relative to radio-powerful AGNs, this suggests that such processes could collectively provide a viable alternative triggering mechanism to mergers for radio-intermediate HERGs.

5   SUMMARY AND CONCLUSIONS

Much previous work concerning radio AGNs has focused on those with the highest radio luminosities, due in most part to their ease of detection in the first flux-limited radio surveys. However, deeper surveys have revealed that radio-powerful examples are rare cases in the general population of local radio AGNs, and it has been shown that HERGs with intermediate radio powers can significantly disturb the warm and cool ISM phases of their hosts through jet-driven outflows. Therefore, the jets associated with radio-intermediate HERGs can potentially have a significant effect on the evolution of their host galaxies, and more detailed study is required to establish the properties of the population.

Our deep optical imaging study of a sample of 30 local radio-intermediate HERGs has allowed us to characterise the detailed optical morphologies of their host galaxies for the first time. Our main results are as follows:

• 53 ± 9 per cent (16/30) of the galaxies in the sample show morphological signatures of a past or on-going merger event based on visual inspection by several independent classifiers, a significantly lower proportion ($3.8\,\sigma$) than for the SLRGs of the 2 Jy sample (94 ± 4 per cent).

• Proportionally, the most radio-powerful half of the sample has a $1.5\,\sigma$ higher level of morphological disturbance than the least radio-powerful half − 67 ± 12 per cent (10/15) and 40 ± 13 per cent (6/15), respectively. The exact same proportions are measured when dividing the sample by [OIII] λ5007 luminosity, however, despite no correlation being found between $L_{1.4GHz}$ and $L_{[OIII]}$.

• Eight galaxies in the sample have highly disturbed morphologies or large-scale tidal tails, suggestive of major galaxy interactions. It is found that all of these galaxies lie in the most radio-powerful half of the sample (a 3.3σ result), including the three galaxies with the highest radio powers. In contrast, 5 out of 8 of these galaxies lie in the half of the sample with the highest [OIII] λ5007 luminosities and 3 out of 8 in the lower half, a difference of only 0.8σ.

• Results from detailed light profile modelling and visual classification indicate that the host galaxies of radio-intermediate AGNs have mixed morphological types. Many show signs of strong disk components (50 per cent; 15/30) in the models, and the majority of multi-component fits are

disk-dominated (53 per cent; 8/15) with a median B/D ~ 0.8. This contrasts with the predominantly early-type host galaxies of traditionally radio-powerful AGNs.

Taken together, these results suggest that the relative importance of triggering HERG activity through galaxy mergers and interactions reduces with radio power. However, mergers appear to remain important for triggering HERGs with higher radio powers, even within the radio-intermediate population. Moving to lower radio powers, the lower proportion of interaction signatures suggests a reduced importance for merger-based triggering. Given the higher proportion of late-type galaxy morphologies in the radio-intermediate population, this could be associated with an increased importance for secular triggering mechanisms related to galaxy disks (e.g. disk instabilities, the action of bars).

In future work we will expand this study to a larger sample of radio-intermediate HERGs, including objects at the higher end of the intermediate radio power range ($L_{1.4\text{GHz}} = 10^{24}$–$10^{25}$ W Hz^{-1}). In this way we will further investigate the radio power dependence of the AGN triggering mechanism. This analysis will also be performed for a matched control sample of galaxies observed in the same way, to allow for direct comparison with non-active galaxies. In addition, we will use high-resolution VLA observations to determine the detailed radio properties of a subset of our sources, and hence greatly improve the general characterisation of this relatively unstudied population of radio AGNs.

REFERENCES

Abazajian K. N., et al., 2009, ApJS, 182, 543
Adams T. F., 1977, ApJS, 33, 19
Atkinson A. M., Abraham R. G., Ferguson A. M. N., 2013, ApJ, 765, 28
Bamford S. P., et al., 2009, MNRAS, 393, 1324
Becker R. H., White R. L., Helfand D. J., 1995, ApJ, 450, 559
Bertin E., 2006, in Gabriel C., Arviset C., Ponz D., Enrique S., eds, Astronomical Society of the Pacific Conference Series Vol. 351, Astronomical Data Analysis Software and Systems XV. p. 112
Bertin E., Arnouts S., 1996, A&AS, 117, 393
Best P. N., Heckman T. M., 2012, MNRAS, 421, 1569
Best P. N., Kauffmann G., Heckman T. M., Ivezić Ž., 2005a, MNRAS, 362, 9
Best P. N., Kauffmann G., Heckman T. M., Brinchmann J., Charlot S., Ivezić Ž., White S. D. M., 2005b, MNRAS, 362, 25
Best P. N., Kaiser C. R., Heckman T. M., Kauffmann G., 2006, MNRAS, 368, L67
Best P. N., von der Linden A., Kauffmann G., Heckman T. M., Kaiser C. R., 2007, MNRAS, 379, 894
Bournaud F., et al., 2012, ApJ, 757, 81
Bower R. G., Benson A. J., Malbon R., Helly J. C., Frenk C. S., Baugh C. M., Cole S., Lacey C. G., 2006, MNRAS, 370, 645
Buttiglione S., Capetti A., Celotti A., Axon D. J., Chiaberge M., Macchetto F. D., Sparks W. B., 2010, A&A, 509, A6
Cabrera-Vives G., Miller C. J., Schneider J., 2018, preprint, (arXiv:1811.03577)
Calzetti D., et al., 2010, ApJ, 714, 1256
Chilingarian I. V., Melchior A.-L., Zolotukhin I. Y., 2010, MNRAS, 405, 1409
Cid Fernandes R., Stasińska G., Schlickmann M. S., Mateus A., Vale Asari N., Schoenell W., Sodré L., 2010, MNRAS, 403, 1036
Condon J. J., Cotton W. D., Greisen E. W., Yin Q. F., Perley R. A., Taylor G. B., Broderick J. J., 1998, AJ, 115, 1693
Croton D. J., et al., 2006, MNRAS, 365, 11
Croton D. J., et al., 2016, ApJS, 222, 22
Driver S. P., et al., 2016, MNRAS, 455, 3911
Duc P.-A., et al., 2015, MNRAS, 446, 120
Dunlop J. S., McLure R. J., Kukula M. J., Baum S. A., O'Dea C. P., Hughes D. H., 2003, MNRAS, 340, 1095
Fabian A. C., 1994, ARA&A, 32, 277
Falomo R., Bettoni D., Karhunen K., Kotilainen J. K., Uslenghi M., 2014, MNRAS, 440, 476
Floyd D. J. E., Kukula M. J., Dunlop J. S., McLure R. J., Miller L., Percival W. J., Baum S. A., O'Dea C. P., 2004, MNRAS, 355, 196
Fukugita M., Ichikawa T., Gunn J. E., Doi M., Shimasaku K., Schneider D. P., 1996, AJ, 111, 1748
Galloway M. A., et al., 2015, MNRAS, 448, 3442
Gao H., Ho L. C., 2017, ApJ, 845, 114
Hardcastle M. J., Evans D. A., Croston J. H., 2007, MNRAS, 376, 1849
Harrison C. M., Thomson A. P., Alexander D. M., Bauer F. E., Edge A. C., Hogan M. T., Mullaney J. R., Swinbank A. M., 2015, ApJ, 800, 45
Heckman T. M., Best P. N., 2014, ARA&A, 52, 589
Heckman T. M., Smith E. P., Baum S. A., van Breugel W. J. M., Miley G. K., Illingworth G. D., Bothun G. D., Balick B., 1986, ApJ, 311, 526
Heckman T. M., Kauffmann G., Brinchmann J., Charlot S., Tremonti C., White S. D. M., 2004, ApJ, 613, 109
Holt J., Tadhunter C. N., Morganti R., 2008, MNRAS, 387, 639
Hopkins P. F., Quataert E., 2010, MNRAS, 407, 1529
Inskip K. J., Tadhunter C. N., Morganti R., Holt J., Ramos Almeida C., Dicken D., 2010, MNRAS, 407, 1739
Kauffmann G., et al., 2003, MNRAS, 346, 1055
Kauffmann G., Heckman T. M., Best P. N., 2008, MNRAS, 384, 953
Kewley L. J., Groves B., Kauffmann G., Heckman T., 2006, MNRAS, 372, 961
Kormendy J., Kennicutt Jr. R. C., 2004, ARA&A, 42, 603
Lintott C. J., et al., 2008, MNRAS, 389, 1179
Lintott C., et al., 2011, MNRAS, 410, 166
Matthews T. A., Morgan W. W., Schmidt M., 1964, ApJ, 140, 35
McNamara B. R., Nulsen P. E. J., 2007, ARA&A, 45, 117
Menci N., Gatti M., Fiore F., Lamastra A., 2014, A&A, 569, A37
Mingo B., Hardcastle M. J., Croston J. H., Dicken D., Evans D. A., Morganti R., Tadhunter C., 2014, MNRAS, 440, 269

Monet D. G., et al., 2003, AJ, 125, 984

Morganti R., Oosterloo T. A., Tadhunter C. N., van Moorsel G., Emonts B., 2005a, A&A, 439, 521

Morganti R., Tadhunter C. N., Oosterloo T. A., 2005b, A&A, 444, L9

Moshir M., Kopman G., Conrow T. A. O., 1992, IRAS Faint Source Survey, Explanatory supplement version 2

Mullaney J. R., Alexander D. M., Goulding A. D., Hickox R. C., 2011, MNRAS, 414, 1082

Mullaney J. R., Alexander D. M., Fine S., Goulding A. D., Harrison C. M., Hickox R. C., 2013, MNRAS, 433, 622

Murphy E. J., et al., 2011, ApJ, 737, 67

Nesvadba N. P. H., Lehnert M. D., Eisenhauer F., Gilbert A., Tecza M., Abuter R., 2006, ApJ, 650, 693

Nesvadba N. P. H., et al., 2010, A&A, 521, A65

Peng C. Y., Ho L. C., Impey C. D., Rix H.-W., 2002, AJ, 124, 266

Peng C. Y., Ho L. C., Impey C. D., Rix H.-W., 2010, AJ, 139, 2097

Popesso P., Biviano A., 2006, A&A, 460, L23

Quinn P. J., 1984, ApJ, 279, 596

Ramos Almeida C., Tadhunter C. N., Inskip K. J., Morganti R., Holt J., Dicken D., 2011, MNRAS, 410, 1550

Ramos Almeida C., et al., 2012, MNRAS, 419, 687

Ramos Almeida C., Bessiere P. S., Tadhunter C. N., Inskip K. J., Morganti R., Dicken D., González-Serrano J. I., Holt J., 2013, MNRAS, 436, 997

Ramos Almeida C., Piqueras López J., Villar- Martín M., Bessiere P. S., 2017, MNRAS, 470, 964

Russell H. R., et al., 2017, MNRAS, 472, 4024

Sadler E. M., Ekers R. D., Mahony E. K., Mauch T., Murphy T., 2014, MNRAS, 438, 796

Schirmer M., 2013, ApJS, 209, 21

Schlegel D. J., Finkbeiner D. P., Davis M., 1998, ApJ, 500, 525

Smith E. P., Heckman T. M., 1989a, ApJS, 69, 365

Smith E. P., Heckman T. M., 1989b, ApJ, 341, 658

Tadhunter C., 2016, A&ARv, 24, 10

Tadhunter C. N., Morganti R., Robinson A., Dickson R., Villar-Martin M., Fosbury R. A. E., 1998, MNRAS, 298, 1035

Tadhunter C., et al., 2011, MNRAS, 412, 960

Tadhunter C., Morganti R., Rose M., Oonk J. B. R., Oosterloo T., 2014, Nature, 511, 440

Tal T., van Dokkum P. G., Nelan J., Bezanson R., 2009, AJ, 138, 1417

Toomre A., Toomre J., 1972, ApJ, 178, 623

Urbano-Mayorgas J. J., et al., 2019, MNRAS, 483, 1829

Villar-Martín M., et al., 2017, MNRAS, 472, 4659

Vogelsberger M., et al., 2014, MNRAS, 444, 1518

Willett K. W., et al., 2013, MNRAS, 435, 2835

Zhao Y.-H., Huang J.-S., Ashby M., Fazio G., Miyazaki S., 2009, Research in Astronomy and Astrophysics, 9, 1061

APPENDIX A: CONTAMINATION BY STAR FORMING GALAXIES

Given the moderate radio powers considered, the contamination of our radio-intermediate AGN sample by radio-quiet AGNs lying within star forming galaxies is possible, and must be considered. The level of this contamination is assessed here.

When generating their local radio AGN sample, Best & Heckman (2012) used the optical properties of the SDSS radio sources to perform three separate tests to distinguish between radio emission arising from star formation and from radio-loud AGN activity: i) the 'D$_{4000}$ versus L_{rad}/M'

method of Best et al. (2005a); ii) the 'BPT' method of Kauffmann et al. (2003); iii) the '$L_{H\alpha}$ versus L_{rad}' method of Kauffmann et al. (2008). These tests are discussed in detail in their Appendix A, along with how their outcomes were used to determine whether the radio emission originated from star formation or AGN activity. We note that *all* of the galaxies in our sample were deemed by Best & Heckman (2012) to have radio emission dominated by radio-loud AGN activity on this basis.

In addition, we perform an alternative test using the estimated star formation rates (SFRs) calculated for the 6 out of 30 galaxies (20%) that are detected in at least one waveband as part of the Infrared Astronomical Satellite (IRAS) Faint Source Survey (Moshir et al. 1992). The SFRs were calculated using the measured IRAS 60μm and 100μm fluxes, following the method of Calzetti et al. (2010). For the 2 out of these 6 galaxies not detected at 100μm, the average 60μm to 100μm flux ratio for the other four galaxies was used in the calculations where necessary. The estimated radio emission at 1.4 GHz resulting from galaxies with these SFRs was then derived using the prescription of Murphy et al. (2011). From this, it is found that star formation could account for an average of only ∼20% of the 1.4 GHz luminosity obtained from the NVSS fluxes for the six galaxies considered − for 5 out of the 6 galaxies, the contribution is ≲30%, with the other (J0838) having the highest possible contribution, at ∼50%. The results of this process are summarised in Table A1.

However, as shown by e.g. Mullaney et al. (2011), the infrared emission in the region of the spectrum covered by IRAS data could be subject to a significant contribution from AGN-heated dust emission, suggesting that the SFRs derived above are unreliable and should be treated as upper limits. In addition, we stress that 80% of the galaxies in the sample do not have IRAS detections in the Faint Source Survey, and would thus have lower relative contributions towards the radio emission from star formation than those reported here. Given the low catalog detection rate and the likely overestimates of the 1.4 GHz luminosities due to star formation for those that are detected, we argue that radio emission from radio-loud AGN activity provides the dominant contribution in all cases, supporting the results of the tests at optical wavelengths. Thus, it is deemed unlikely that there is significant contamination of our radio AGN sample by radio-quiet AGNs in star forming galaxies.

This paper has been typeset from a TEX/LATEX file prepared by the author.

Table A1. Star formation properties for the six galaxies in the sample with far-infrared detections in the IRAS Faint Source Survey (Moshir et al. 1992). The target IDs and 60μm fluxes are presented, along with estimations of the star formation rates (following Calzetti et al. 2010). The ratio of the expected resultant 1.4 GHz luminosity (following Murphy et al. 2011) to that derived from the NVSS fluxes is displayed in the final column.

Target ID	$F_{60\mu m}$ (Jy)	Star formation rate $(M_\odot \, yr^{-1})$	$\frac{L^{SF}_{1.4GHz}}{L^{NVSS}_{1.4GHz}}$
J0810	0.685	33.2	0.10
J0838	0.628	13.7	0.52
J0950	0.410	5.94	0.04
J1108	0.487	20.5	0.28
J1243	0.449	29.0	0.20
J1609	0.856	8.76	0.14